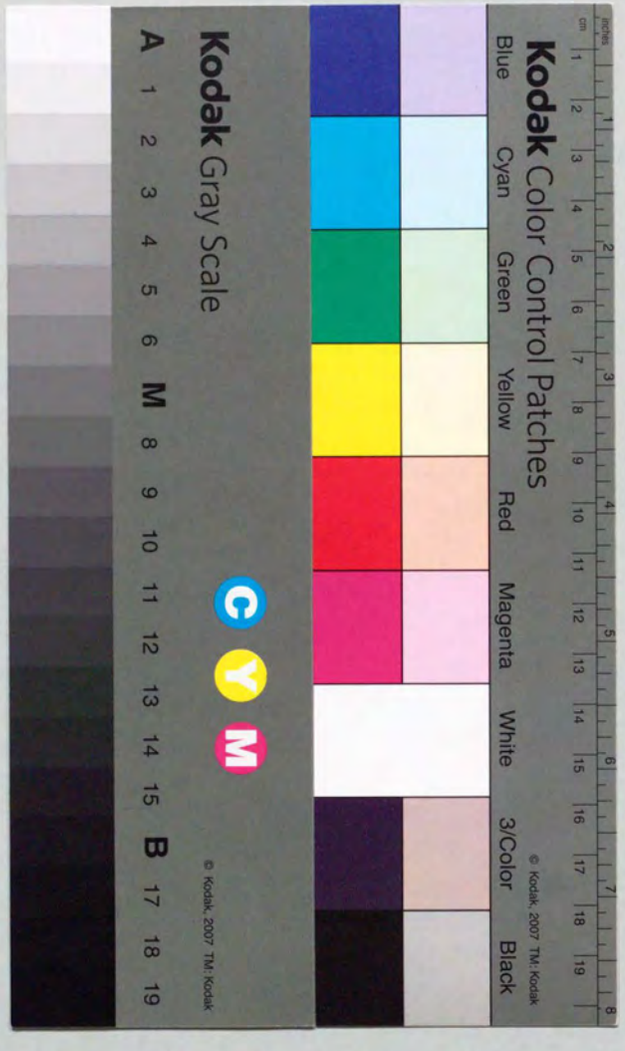

学位論文

Mesoscopic Phenomena in Quantum Wires

（量子細線におけるメソスコピックな輸送現象）

平成４年１２月博士（理学）申請

東京大学大学院理学系研究科
物理学専攻
田　村　浩　之

Thesis

Mesoscopic Phenomena in Quantum Wires

Hiroyuki Tamura

Institute for Solid State Physics
University of Tokyo

December 1992

Acknowledgments

Over the course of working on this thesis, there have been many people who have helped me along my path. It is great pleasure to acknowledge their contributions.

I would like to express my sincerest gratitude to Professor Tsuneya Ando for his continual guidance and encouragement throughout the course of the present work and his critical reading of the manuscript. I appreciate Professor Hiroshi Akera, Dr. Hideo Yoshioka, and Dr. Masahito Ueda for useful advice and discussion. I wish to thank Professor Hidetoshi Fukuyama for encouragement and valuable discussions, and I also thank Mrs. Shizue Maruyama and all other members of the research group under Professor T. Ando and Professor H. Fukuyama for help and many interesting conversations.

Finally I would like to express special gratitude to my wife Noriko Handa for help and continual encouragement during the last year of the doctor course. I dedicate this thesis to my parents to express deep gratitude for thier support and encouragement for years.

Contents

Chapter 1
Introduction

Recent developments in the fabrication technology of submicrometer structures have revealed a quantum-mechanical nature of electrical transports at low temperatures. In very small systems and at low temperatures, the phase-coherence length becomes larger than the sample size, *i.e.*, electrons can move without the loss of their memory of quantum-mechanical phase. Various quantum effects can be observed in these systems of *mesoscopic* size, in which the system size is much larger than the atomic (= microscopic) scale but smaller than that of the macroscopic system where there is no phase coherence.

One of the most interesting mesoscopic phenomena is the conductance fluctuations. Conductance fluctuations were unexpectedly observed in the magnetoresistance of a small normal-metal ring [1], instead of the Aharanov-Bohm oscillations predicted theoretically [2-4] and observed later [5]. Conductance fluctuations with the Aharanov-Bohm effect are shown in Fig. 1. A special feature of the conductance fluctuations is that, although the fluctuating patterns are random as a function of a magnetic field B or the Fermi energy E_F, they are time-independent, reproducible, and specific to the impurity-configuration in each sample. We can understand this feature by regarding the electron conduction as a random walk in a disordered sample: When an electron passes through the system, it is scattered many times by the elastic impurity-scattering. The superposition of all the Feynman paths, each of which have a different phase, leads to random patterns in the conductance as a function of B or E_F.

Diagrammatic perturbation calculations [6-11] have shown that the amplitude of the fluctuation takes a universal value of order e^2/h (the universal conductance fluctuation), independent of the sample size and degree of disorder at zero temperature in *metallic* samples. In metallic samples, all the sample dimensions are always much larger than the mean free path l and the Fermi wavelength λ_F, and are much smaller than the localization length ξ. The universal conductance fluctuation in metallic samples has been shown by various other methods both analytically [12-16] and numerically [17-27].

Another interesting mesoscopic phenomenon is persistent currents in small rings. Persistent currents are dissipationless equilibrium currents which flow in an isolated

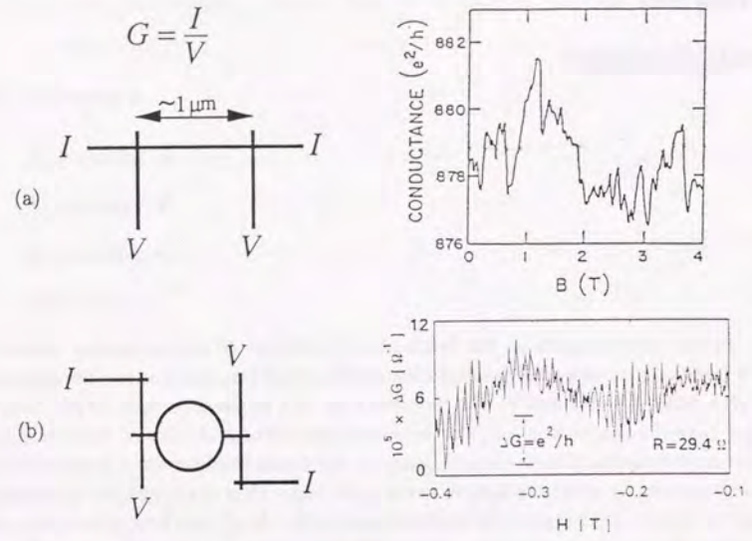

Fig. 1 Conductance fluctuations measured in a (a) wire and (b) ring geometry as a function of a magnetic field. The fluctuating patterns are random but sample-specific, and these patterns are reproducible if we sweep the magnetic field down from a high field. In the wire, both the value of conductance and the periodicity are random. In the ring geometry, the value of conductance is random, but the fluctuating pattern with a periodicity h/e can be clearly seen, which is the evidence of the Aharanov-Bohm effect.

ring induced by a static magnetic flux ϕ inside the ring shown in Fig. 2. Equilibrium persistent currents in normal metallic rings were first predicted by Büttiker, Imry and Landauer [28-30]. Experimental observation of the persistent currents was first made by Levy *et al.* [31] in the magnetization response of 10^7 isolated Cu rings at a low temperature. Recently another experiment was done by Chandrasekhar *et al.* [32] in a *single* Au ring. So far none of existing theories [33-43] can explain completely these experimental results. Especially the magnitudes of persistent currents observed in the experiments are larger than those predicted by most theories. (A review of works on persistent currents will be given in Chapter 5.)

In addition to the interference effects mentioned above, the quantum size effect becomes important in semiconducting materials, where the sample size is smaller than the mean free path l and is larger but comparable to the Fermi wavelength λ_F. When we

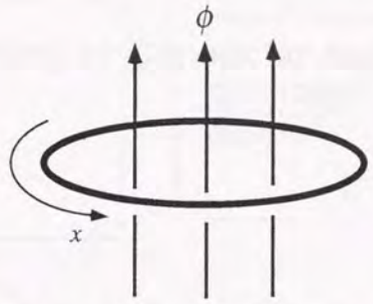

Fig. 2 One-dimensional ring with a circumference of L in the x direction. The ring is threaded by a static magnetic flux ϕ.

consider a *quantum wire* where the wire width $W \ll l$ and $W \gtrsim \lambda_F$, the one-dimensional (1D) subbands are well-defined, because their level broadening is much smaller than their energy separations. When the sample length L is shorter than the mean free path (called *ballistic* region), an electron can move without suffering from impurity-scattering and quantum size effects are clearly seen. One of the typical phenomena is the conductance quantization across a narrow point contact [44, 45]. Electrons in the two-dimensional system at a $GaAs/Al_xGa_{1-x}As$ heterostructure can pass through a narrow point contact formed by application of a negative bias voltage to the split metallic gates on the top of the 2D heterostructure.

The conductance $G = I/V$ across the point contact was observed to be quantized in units of $e^2/\pi\hbar$ as shown in Fig. 3. Discrete energy-levels (also called *subbands* or *channels*) are formed in the point contact region due to confinement potential in the lateral direction. As the bias voltage is increased, the bottom of confinement potential goes down, and the number of channels M at the Fermi energy in the narrowest part of the contact of width $W^{\min}$ is increased. The conductance is calculated by $G = (e^2/\pi\hbar)\sum_{i,j=1}^{N} |t_{ij}|^2$, where t_{ij} is the transmission amplitude of an electron from a channel i to j and $N(> M)$ is the total number of incoming and outgoing channels. When we assume an adiabatic limit for simplicity (although not the actual situation in the experiments), the effective potential for the channel i is given by $U_i^{\max} = (\hbar^2/2m)(\pi i/W^{\min})^2$. Electrons in the channel satisfying $U_i^{\max} < E_F$ are transmitted with probability unity, *i.e.*, $t_{ii} = 1$, electrons in the channel satisfying $U_i^{\max} > E_F$ are reflected with probability unity, *i.e.*, $t_{ii} = 0$, and scattering between different channels is completely neglected, *i.e.*, $t_{ij} = 0$ for $i \neq j$. This leads to the quantized conductance $G = M(e^2/\pi\hbar)$.

In quantum wires, we can no longer use the idea based on semiclassical Feynman paths valid in metallic wires, even when $L \gg l$. Therefore different behaviors can

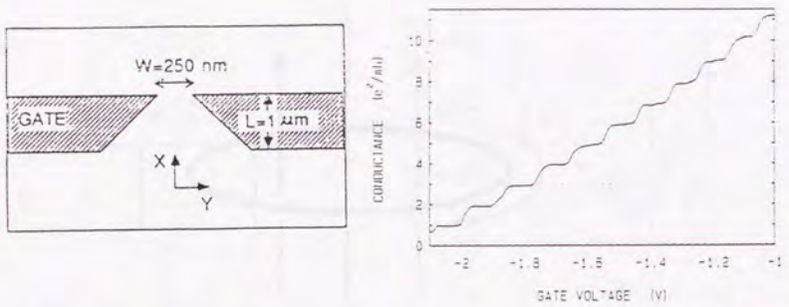

Fig. 3 Quantum point contact and the observed conductance across it as a function of the gate voltage. Due to a negative bias applied to the split gates, two-dimensional electrons beneath the gates are depleted and can pass only through the narrow point contact.

be expected in mesoscopic phenomena such as conductance fluctuation and persistent currents in quantum wires. Moreover the localization effect can play an important role. As a matter of fact, in a strictly 1D system, the localization length ξ is essentially equal to the mean free path l and therefore there is no diffusive region where the conventional perturbational treatment is valid.

The purpose of this paper is to study typical mesoscopic phenomena, like conductance fluctuations in quantum wires and persistent currents in a quantum ring. In the study of conductance fluctuations, we use several methods of calculation, *i.e.*, numerical, perturbational, and distribution-function method, and try to reach a full understanding of the conductance fluctuation in quantum wires. In the study of persistent currents, we apply the conventional diagrammatic technique and examine the influence of well-defined subbands on the magnitude of persistent currents.

This thesis is organized as follows. In Chapter 2 we study numerically the conductance fluctuation in quantum wires. The effects of a magnetic field, spin-orbit interaction, and boundary roughness scattering are taken into account. In Chapter 3 we use the diagrammatic perturbation theory and study electrical transport in quantum wires. We calculate the conductance, the weak localization correction, and the conductance fluctuation. In Chapter 4 we try to derive the Fokker-Planck equation for the distribution function for the conductance. The conductance, its fluctuation, and the localization length can be obtained from the derived equation, and the calculated results are compared with those obtained in Chapters 2 and 3. In Chapter 5 we calculate persistent currents in a quantum ring by use of the diagrammatic technique and we examine the effect of subbands in a quantum ring. Finally we give a summary in Chapter 6.

Chapter 2
Numerical Study of Conductance Fluctuation

In this chapter we study the conductance fluctuation in quantum wires and the effect of localization on it by a numerical calculation [27, 46-49]. In the study of the fluctuation and the localization, it is very important to consider the symmetry of the system and the kind of scatterers. We take into account the effect of a magnetic field, spin-orbit scattering, and boundary roughness. We describe the theoretical formulation for the scattering matrix in Sec. 2.1, present numerical results in Sec. 2.2, and give a summary in Sec. 2.3..

2.1 Scattering Matrix Formulation

We consider a two-dimensional system of non-interacting electrons confined within the width W in the lateral (y) direction in the presence of a perpendicular magnetic field $\mathbf{B}$ and in the absence of spin-orbit scatterings and boundary roughness scatterings. (As will be discussed in Sec. 2.1 D and E, the effect of spin-orbit scatterings and boundary roughness scatterings can be easily treated by a lattice model rather than a continuum model described below.) The Hamiltonian is written as

$$H = \frac{1}{2m}(\mathbf{p}+e\mathbf{A})^2+U(y)+V(\mathbf{r}), \quad U(y) = \begin{cases} 0 & -W/2<y<W/2 \\ \infty & \text{otherwise} \end{cases}, \tag{2.1}$$

where $\mathbf{r} = (x, y)$, $\mathbf{A} = (-By, 0)$, m is the effective mass, and $V(\mathbf{r})$ is the scattering potential. The system has length L in the x direction and is connected on both ends to long perfect leads which themselves are connected to reservoirs. We assume the scattering potential of a single impurity as a δ function with the same strength $|\gamma|$. In low-mobility wires, this model of impurity with a short-range potential is expected to simulate a (screened) ionized impurity and roughness at the heterointerface of GaAs and $Al_xGa_{1-x}As$, although the dominant scattering mechanism in high-mobility narrow wires is believed to have a long-range potential [50, 51] and the mobility of electrons becomes larger than that in 2D systems [52].

In the absence of impurities the wavefunction is written as

$$\xi(\mathbf{r}) \propto e^{ikx}\psi(y)\,, \tag{2.2}$$

where $\psi(y)$ satisfies the reduced equation

$$\left[-\frac{\hbar^2}{2m}\frac{d^2}{dy^2} + \frac{m}{2}\omega_c^2(y - l_B^2 k)^2 + U(y)\right]\psi(y) = E\psi(y)\,, \tag{2.3}$$

with $\omega_c = eB/m$ and $l_B^2 = \hbar/eB$. For a given energy ($E = E_F$) we obtain the two kinds of mode, the "conducting mode" whose wavenumber is real, $\pm k_n$ ($n = 1, \cdots, N_c$; $k_n > 0$), and the "evanescent mode " whose wavenumber is imaginary, $\pm i\kappa_n$ ($n = N_c+1, \cdots, \infty$; $\kappa_n > 0$). We denote the right-going waves consisting of the conducting modes with $+k_n$ or the evanescent modes with $i\kappa_n$ as ξ_{n+} and the left-going waves with $-k_n$ or $-i\kappa_n$ as ξ_{n-}.

The normalization of the conducting solution $\xi_{n\pm}$ is chosen as

$$\xi_{n\pm}(\mathbf{r}) = \frac{1}{\sqrt{v_n}} e^{\mp ik_n x}\psi_{n\pm}(y)\,, \tag{2.4}$$

with the velocity in the x direction of the nth state given by

$$v_n = \frac{\hbar}{m}\int dy\ \psi_{n+}^*(y)\Big(k_n - \frac{y}{l_B^2}\Big)\psi_{n+}(y), \tag{2.5}$$

so that each channel carries a unit flux. The normalization of the wavefunction of the evanescent channel is arbitrary and the conductance is independent of their choices.

The wavefunction can be written for the incoming wave from the left side of the scattering region $[0, L]$ as

$$\Psi_n^+(x,y) = \begin{cases} \xi_{n+} + \sum_{n'}^{N} \xi_{n'-} r_{n'n} & \text{for } x < 0\,, \\ \sum_{n'}^{N} \xi_{n'+} t_{n'n} & \text{for } x > L\,, \end{cases} \tag{2.6}$$

where t_{mn} and r_{mn} are the transmission and reflection amplitudes, respectively, and for the incoming wave from the right side of the scattering region as

$$\Psi_n^-(x,y) = \begin{cases} \xi_{n-} + \sum_{n'}^{N} \xi_{n'+} r'_{n'n} & \text{for } x > L\,, \\ \sum_{n'}^{N} \xi_{n'-} t'_{n'n} & \text{for } x < 0\,, \end{cases} \tag{2.7}$$

with transmission and reflection amplitudes, t'_{mn} and r'_{mn}. The scattering matrix or the S matrix is defined as

$$S = \begin{bmatrix} r & t' \\ t & r' \end{bmatrix}. \tag{2.8}$$

The current conservation law requires the unitarity of the S matrix as

$$\tilde{S}^\dagger \tilde{S} = \tilde{S}\tilde{S}^\dagger = 1\,, \tag{2.9}$$

where $\tilde{S}$ consists of the $N_c \times N_c$ transmission matrices $\tilde{t}$ and $\tilde{t}'$ and the reflection matrices $\tilde{r}$ and $\tilde{r}'$, which contain the scattering amplitudes from N_c incoming conducting channels to N_c outgoing conducting channels.

To calculate the conductance between two reservoirs, we use the two-terminal, multi-channel version [53-57] of Landauer's formula [58]

$$G = \frac{2e^2}{h}\mathrm{Tr}\,(\tilde{t}\tilde{t}^\dagger) = \frac{2e^2}{h}\sum_{n=1}^{N_c}\sum_{m=1}^{N_c}|\tilde{t}_{mn}|^2\,, \tag{2.10}$$

where a factor 2 due to the spin degeneracy is included. Here it should be noted that conductance fluctuations, though universal in the two-terminal metallic wire, can exceed the universal value by many orders of magnitude in the multi-terminal system, as shown theoretically [59-62] and experimentally [63, 64].

The overall S matrix for the disordered region $L \times W$ containing a certain number of impurities with δ-potential can be obtained by a decomposition into single-impurity parts and free-propagating parts using a composition law [65]. If we consider the two S matrices defined by

$$S_1 = \begin{bmatrix} r_1 & t'_1 \\ t_1 & r'_1 \end{bmatrix} \quad \text{and} \quad S_2 = \begin{bmatrix} r_2 & t'_2 \\ t_2 & r'_2 \end{bmatrix}, \tag{2.11}$$

then the composed S matrix $S_{12} \equiv S_1 \otimes S_2$ for S_1 and S_2 in series can be calculated as

$$\begin{aligned} t_{12} &= t_2\big[1 - r'_1 r_2\big]^{-1} t_1\,, \\ t'_{12} &= t'_1\big[1 - r_2 r'_1\big]^{-1} t'_2\,, \\ r_{12} &= r_1 + t'_1 r_2\big[1 - r'_1 r_2\big]^{-1} t_1\,, \\ r'_{12} &= r'_2 + t_2 r'_1\big[1 - r_2 r'_1\big]^{-1} t'_2\,. \end{aligned} \tag{2.12}$$

Note that the composition law satisfies the associative law $(S_1 \otimes S_2) \otimes S_3 = S_1 \otimes (S_2 \otimes S_3)$, but does not satisfy the commutative law in general, *i.e.*, $S_2 \otimes S_1 \neq S_1 \otimes S_2$. The overall S matrix can be expressed as

$$S = S_1^{\mathrm{free}} \otimes S_1^{\mathrm{imp}} \otimes S_2^{\mathrm{free}} \otimes \cdots \otimes S_{N_I}^{\mathrm{imp}} \otimes S_{N_I+1}^{\mathrm{free}}\,, \tag{2.13}$$

where N_I is the total number of impurities. It must be noted that this decomposition method cannot be applied to the system containing impurities with the long-range potential. This is why a lattice model will be used for the study of effects of boundary roughness scattering in Sec. 2.2E.

To derive the S matrix for a single impurity, we integrate the Schrödinger equation for the system containing an impurity with a δ-potential of strength γ at $\mathbf{r}_0 = (x_0, y_0)$ over the infinitesimally small region $[x_0 - \epsilon, x_0 + \epsilon]$ with respect to x. We obtain

$$\frac{\partial}{\partial x}\Psi(x_0+\epsilon, y) - \frac{\partial}{\partial x}\Psi(x_0-\epsilon, y) = \frac{2m\gamma}{\hbar^2}\delta(y - y_0)\Psi(x_0, y)\,. \tag{2.14}$$

Further the continuity of the wavefunction at $x=x_0$ leads to

$$\Psi(x_0+\epsilon, y) = \Psi(x_0-\epsilon, y)\,. \tag{2.15}$$

The wavefunction $\psi_{n\pm}(y)$ is expanded by an orthonormal set of the N eigenstates φ_j's of the reduced Hamiltonian for $B=0$.

$$\psi_{n\pm}(y) = \sum_{j=1}^{N} \varphi_j(y)\, c_{jn}^{\pm} \tag{2.16}$$

with

$$\varphi_j(y) = \begin{cases} \sqrt{\frac{2}{W}} \sin\left(\frac{\pi j}{W}(y+\frac{W}{2})\right) & \text{for } -\frac{W}{2} \le y \le \frac{W}{2}\,, \\ 0 & \text{otherwise.} \end{cases} \tag{2.17}$$

Substituting Eqs. (2.6) and (2.16) into Eqs. (2.14) and (2.15), multiplying $\varphi_{j'}^*(y)$, and integrating with respect y, we have the transmission and reflection matrix, t and r, for incoming waves from the left hand side

$$\begin{bmatrix} C_-K+i\Gamma C_- & C_+K+i\Gamma C_+ \\ -C_- & C_+ \end{bmatrix} \begin{bmatrix} r \\ t \end{bmatrix} = \begin{bmatrix} C_+K-i\Gamma C_+ \\ C_+ \end{bmatrix}\,, \tag{2.18}$$

with

$$(C_\pm)_{jn} = c_{jn}^{\mp}\sqrt{\frac{\pi\hbar}{mWv_n}},\quad (K)_{nn'} = \frac{k_n W}{\pi}\delta_{nn'},\quad (\Gamma)_{jj'} = \frac{m\gamma W}{\pi\hbar^2}\varphi_j(y_0)^*\varphi_{j'}(y_0). \tag{2.19}$$

In the same way we can obtain the transmission and reflection matrix, t' and r', for incoming waves from the right side as

$$\begin{bmatrix} C_-K+i\Gamma C_- & C_+K+i\Gamma C_+ \\ -C_- & C_+ \end{bmatrix} \begin{bmatrix} t' \\ r' \end{bmatrix} = \begin{bmatrix} C_-K-i\Gamma C_- \\ -C_- \end{bmatrix}\,. \tag{2.20}$$

Combining Eqs. (2.18) and (2.20), we finally obtain

$$S^{\rm imp} = \begin{bmatrix} C_-K+i\Gamma C_- & C_+K+i\Gamma C_+ \\ -C_- & C_+ \end{bmatrix}^{-1} \begin{bmatrix} C_+K-i\Gamma C_+ & C_-K-i\Gamma C_- \\ C_+ & -C_- \end{bmatrix}. \tag{2.21}$$

The S matrix for the free propagation from $x=x_0$ to $x=x_0+\Delta x$ is given by

$$S^{\rm free} = \begin{bmatrix} 0 & \theta \\ \theta & 0 \end{bmatrix}\,,\quad (\theta)_{nn'} = e^{ik_n\Delta x}\delta_{nn'}\,. \tag{2.22}$$

The wavenumbers $\pm k_n$ or $\pm i\kappa_n$ and the corresponding wavefunctions $\mathbf{c}_n^{\pm}$ are calculated as follows [66]: Substituting Eq. (2.16) into Eq. (2.3), we obtain

$$\sum_{j'=1}^{N} \left[E_j\delta_{jj'} + \frac{m}{2}\omega_c^2\langle(y-l_B^2k)^2\rangle_{jj'}\right]c_{j'} = E_F c_j\,, \tag{2.23}$$

with $E_j=(\hbar^2/2m)(\pi j/W)^2$, where

$$\langle Y\rangle_{jj'} = \int dy\varphi_j^*(y) Y \varphi_{j'}(y)\,. \tag{2.24}$$

Defining $d_j=(kW/\pi)c_j$, Eq. (2.23) can be rewritten as

$$\begin{bmatrix} 0 & 1 \\ A & B \end{bmatrix}\begin{bmatrix} c \\ d \end{bmatrix} = \frac{kW}{\pi}\begin{bmatrix} c \\ d \end{bmatrix}\,, \tag{2.25}$$

with

$$\begin{aligned} (A)_{jj'} &= \left[\left(\frac{k_F W}{\pi}\right)^2 - j^2\right]\delta_{jj'} - \left(\frac{\hbar\omega_c}{2E_1}\right)^2\left\langle\left(\frac{\pi y}{W}\right)^2\right\rangle_{jj'}\,, \\ (B)_{jj'} &= \frac{\hbar\omega_c}{E_1}\left\langle\frac{\pi y}{W}\right\rangle_{jj'}\,, \end{aligned} \tag{2.26}$$

where $k_F=(2mE_F/\hbar^2)^{1/2}$. Solving Eq. (2.25), we obtain $2N$ eigenvalues $\pm k_n$ or $\pm i\kappa_n$ and $2N$ eigenvectors $\mathbf{c}_n^{\pm}$.

The situation becomes particularly simple in the absence of a magnetic field. We have $k_n=[k_F^2-(\pi n/W)^2]^{1/2}$ and $v_n=\hbar k_n/m$ when $E_n<E_F$ and $\kappa_n=[(\pi n/W)^2-k_F^2]^{1/2}$ when $E_n>E_F$. Further, we have $c_{jn}^{\mp}=\delta_{jn}$ and the S matrix (2.21) reduces exactly to the same expression as that previously obtained without evanescent states [23, 24] and with evanescent states [25, 26, 67].

The system is characterized by the following three dimensionless parameters, $2W/\lambda_F$, $l/\lambda_F = E_F\tau/\pi\hbar$, and $\tilde{\gamma} \equiv 2m\gamma/\pi\hbar^2$, where τ is the relaxation time in 2D systems given by $\tau^{-1}=n_i|\gamma|^2m/\hbar^3$ with n_i the impurity concentration and is related to the mean free path through $l=v_F\tau$. The parameter $2W/\lambda_F$ represents the number of occupied subbands at the Fermi energy. The parameter $\tilde{\gamma}$ represents the importance of the higher Born scatterings from a single impurity relative to the first Born effect. In the limit of negligibly small $\tilde{\gamma}$ and large concentration n_i of impurities with a fixed l (the high concentration or white-noise limit), $\tilde{\gamma}$ becomes irrelevant and the system is characterized only by the two parameters $2W/\lambda_F$ and l/λ_F. In the following, except for a single-impurity system, we choose $|\tilde{\gamma}|=0.2$, for which the system is nearly in the high concentration limit. In addition, equal amounts of attractive and repulsive scatterers are distributed in a sample in order to cancel out effects of energy shifts to the lowest order. The number of samples with different impurity configuration is between 2000 and 3000.

The δ-potential can cause some problems. A typical example is a divergence associated with its bound state in the attractive case in two or three dimensional systems. The same happens in the present quantum wire and the binding energy diverges logarithmically if the number N of the basis $\phi_j(y)$ becomes infinite. Any realistic scatterers have a potential with nonzero range. Therefore, we shall introduce a cutoff E_c in such a way that N is determined by the condition $E_N<E_c$. This roughly corresponds to a

cutoff of the potential range at about k_c^{-1} with $\hbar^2 k_c^2/2m \sim E_c$. We shall choose $E_c \simeq 4E_F$ in the numerical examples shown in the following section.

2.2 Numerical Results

A. A Single Impurity

The conductance for a single impurity in the absence of a magnetic field has already been calculated by Bagwell [67]. It has been shown that for an attractive potential a quasi-bound-state is formed below each subband bottom where the transmission probability is reduced considerably. For a repulsive scatterer no such quasi-bound-state appears as is expected. The situation changes drastically in the presence of a magnetic field [68, 69]. The bound-state energy of a single impurity can be obtained as

$$1 = \frac{\gamma}{2\pi l_B^2} \sum_{\nu=0}^{\nu_{\max}} \frac{1}{E-(\nu+1/2)\hbar\omega_c}, \tag{2.27}$$

where $\nu_{\max}$ is a cutoff. This shows that there exist bound states (with an energy larger than each Landau-level energy) even for a repulsive impurity in 2D systems in strong magnetic fields.

An example of the calculated conductance for a single impurity with $\tilde{\gamma} = \pm 0.7$ located at the center of the wire ($y_0 = 0$) in a strong magnetic field ($\hbar\omega_c/E_1 = 10$ or $W/l_B \simeq 7$) is shown in Fig. 4. Dips can be seen both for repulsive and attractive potential. They are due to the suppression of the transmission probability of the highest conducting channels : For example, when two subbands are occupied, we have $|t_{11}| \simeq 1$ and $|t_{12}| \simeq |t_{21}| \simeq |t_{22}| \simeq 0$. The energies of quasi-bound states are close to those obtained from Eq. (2.27) for $\nu_{\max} = 10$ shown in Fig. 4 by the vertical arrows.

The overlap of the wave functions of the highest conducting channels at the position of the impurity, $|\psi^*_{N_c-}(y_0)\psi_{N_c+}(y_0)|$, is also included in the figure. At energies away from those of quasi-bound states, the conductance is nearly quantized except when this overlap is large. A singular peak seen just at the energy of the bottom of the second subband ($E_F \simeq 15E_1$) is due to the presence of a node of the wavefunction at $y_0 = 0$. When E_F becomes slightly larger than the subband bottom, the overlap rapidly increases and the conductance is reduced.

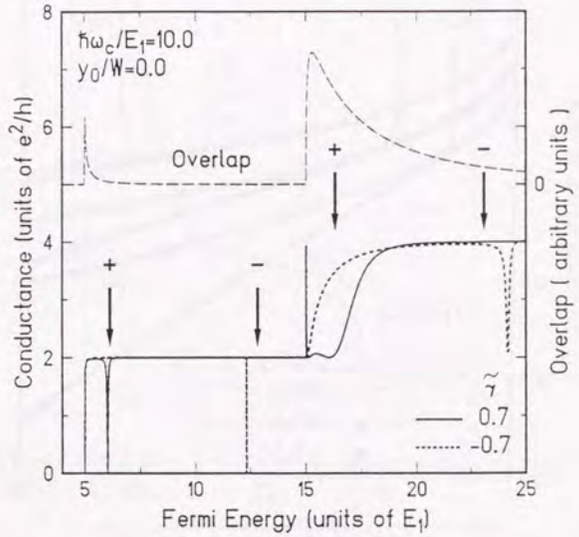

Fig. 4 Conductance for a single impurity with δ-function potential located at the center of wire ($y_0 = 0$) as a function of the Fermi energy in a strong magnetic field. The solid line represents that for a repulsive potential and the dotted line for an attractive potential. The vertical arrows indicate the expected quasi-bound-state energies for a 2D system with '+' for a repulsive potential and '−' for an attractive potential. The overlap between the highest conducting channels at the impurity position, $|\psi^*_{N_c-}(y_0)\psi_{N_c+}(y_0)|$, is represented by the dashed line.

B. Conductance Fluctuation

In Fig. 5 we show the length dependence of the averaged conductance in the absence of a magnetic field. The narrowest wire has 5 occupied subbands and the widest 20 below the Fermi energy. We have assumed $l/\lambda_F = 51.25$, for which the broadening is always smaller than the smallest subband-separation ($\hbar/\tau = (1/\pi)(2W/\lambda_F)^2(\lambda_F/l)E_1 \simeq 0.87 \times (E_2 - E_1)$ even for $2W/\lambda_F = 10.25$) and therefore the subbands are well-resolved. The Fermi level lies in the middle of the two subband bottoms E_{N_c} and E_{N_c+1}. We have used the two different ways of averaging, the arithmetic average $\langle G \rangle$ and the geometric average $\exp[\langle \ln G \rangle]$. With the increase of the sample length, the conductance decreases starting from the quantized value $G = 2N_c e^2/h$. As the system becomes much longer, the conductance begins to decrease exponentially. The localization length ξ can be

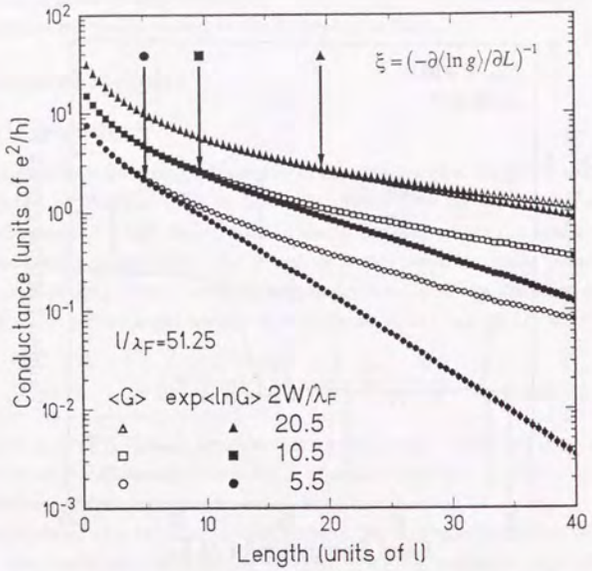

Fig. 5 Conductance as a function of the length L for different wire widths. The number of occupied subbands is $2W/\lambda_F$. The estimated localization lengths are indicated by the vertical arrows. The numerical uncertainty of ξ is smaller than the width of the arrows.

estimated by fitting to $\xi=-(\partial\langle\ln G\rangle/\partial L)^{-1}$ for the region $25<L/l<40$ [70-74]. We have $\xi/l=4.9\pm0.2$ for $N_c=5$, 10.0 ± 0.3 for $N_c=10$, and 19.6 ± 1.0 for $N_c=20$, which are denoted in the figure by the vertical arrows. The two different averages start to deviate from each other when the length exceeds the localization length reflecting the singular, non-Gaussian distribution of the conductance in the localized region $L\gtrsim\xi$ [70-74].

In 1D wires, an exact expression for the distribution function of the conductance was derived by Abrikosov [75] (see also Sec. 4.2) as

$$W(\tilde{s};\rho)=\frac{2}{\sqrt{\pi\tilde{s}^3}}\int_{\mathrm{arch}\sqrt{\rho}}^{\infty}du\,\frac{u\exp\left[-\left(u^2/\tilde{s}+\tilde{s}/4\right)\right]}{\left(\cosh^2 u-\rho\right)^{1/2}},\tag{2.28}$$

where $\tilde{s}\equiv L/\xi=2\alpha L=2L/l$ and $\rho\equiv 1/g$. Fig. 6 shows the exact distribution function in a 1D wire and Fig. 7 gives the conductance and fluctuation as a function of length averaged over the distribution in Fig. 6. There is no length region where the conductance obeys a normal Gaussian distribution and the two different averages of the

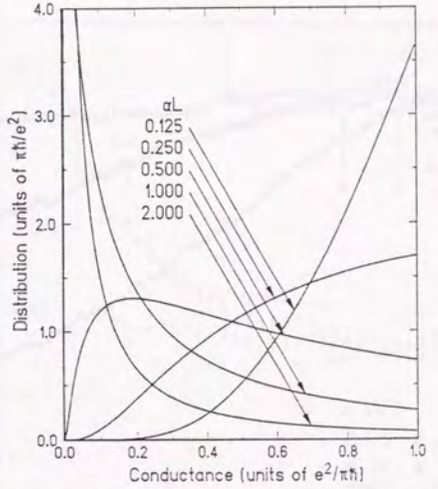

Fig. 6 Exact distribution function of the conductance in 1D wire for several values of $\alpha L=L/2\xi$.

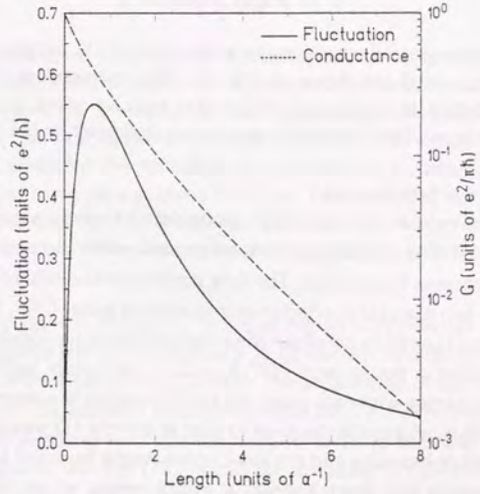

Fig. 7 Exact conductance (dashed line) and fluctuation (solid line) vs length in 1D wire.

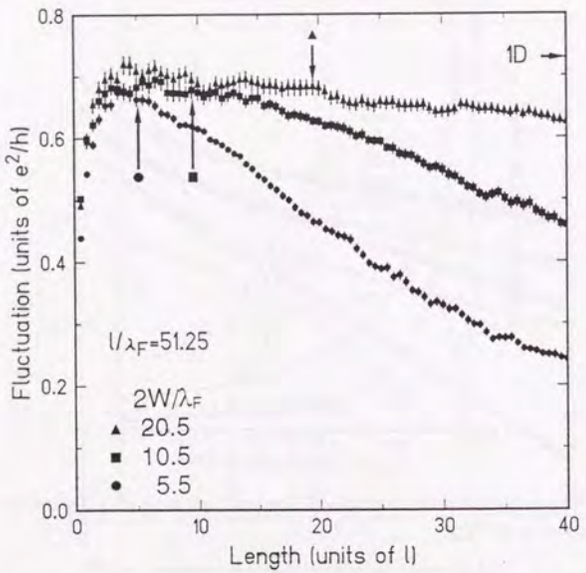

Fig. 8 Conductance fluctuations as a function of the length L for systems corresponding to those shown in Fig. 5. The universal value obtained by the perturbation for quasi-one-dimensional metallic wires is indicated by a horizontal arrow. The localization lengths are indicated by the vertical arrows.

conductance give the same value.

Figure 8 shows the corresponding results for the conductance fluctuation $\delta G \equiv \langle (G - \langle G \rangle)^2 \rangle^{1/2}$. With increasing length, the fluctuation first increases, takes a maximum value, and then begins to decrease. The first increase in the nearly ballistic regime is a reflection of the fact that the conductance is quantized when $L \lesssim l$, and the decrease for $L \gtrsim \xi$ is a result of the reduction of the conductance due to the localization effect. When the channel number is not so large ($2W/\lambda_F = 5.5$), the nearly ballistic regime and the localized regime overlap with each other and the fluctuation is always strongly dependent on the length. This behavior is the same as that in strictly 1D wires shown in Fig. 7. As the channel number increases and the localization length becomes larger, the maximum fluctuation increases and there appears a length region where the fluctuation stays independent of length (the universal region). The maximum fluctuation for $2W/\lambda_F = 20.5$ is close to but slightly smaller than $0.73e^2/h$ derived by the perturbational method for the quasi-one-dimensional metallic wires [8-11]. It will be shown in Chapter 3 and

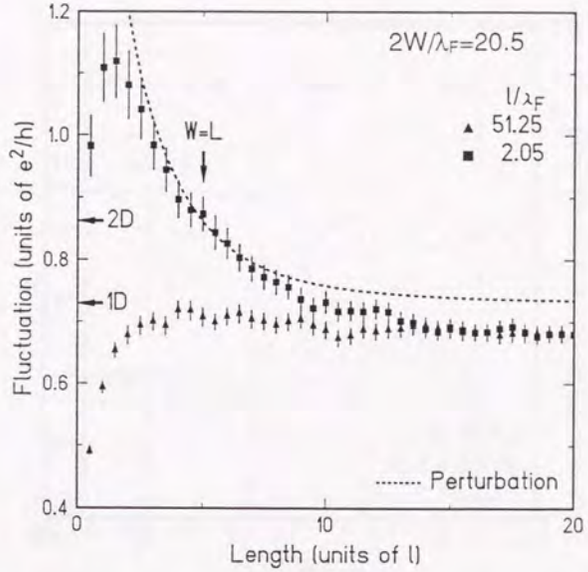

Fig. 9 A crossover of conductance fluctuations from a quantum wire to a metallic wire when the number of the occupied subbands is 20. The solid squares correspond to a wire where the broadening is larger than the level separation and the subband structure is smeared out. The dotted line indicates the result obtained by the perturbation calculation for metallic wires. The triangles are the same data as those in Fig. 8. The vertical arrow indicates the length corresponding to the 2D square. The universal values obtained by the perturbation for quasi-one-dimensional wires and 2D squares are indicated by the horizontal arrows.

4 that the absolute value of δG in the universal region in N-channel quantum wires is the same as that calculated perturbationally in quasi-one-dimensional metallic wires.

A crossover occurs from 1D to 2D when the broadening of the subbands exceeds their separation and the subband structure is smeared out. Figure 9 shows calculated δG for $l/\lambda_F = 2.05$ together with that for $l/\lambda_F = 51.25$ in the case that the number of occupied subbands is 20. For $l/\lambda_F = 2.05$ the situation is closer to that of metallic wires, *i.e.*, the broadening is larger than the largest subband separation ($\hbar/\tau \simeq 1.6 \times (E_{N_c+1} - E_{N_c})$) and the wire width is larger than the mean free path ($W/l = 5$). The numerical result is in good agreement with that by the perturbation represented by the dotted line in the region $2l < L < 10l$ including the length corresponding to the 2D

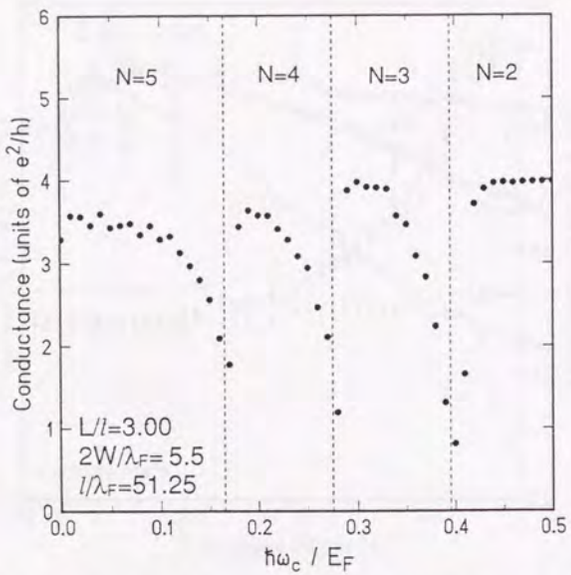

Fig. 10 Conductance as a function of the magnetic field for $L/l = 3$ and $2W/\lambda_F = 5.5$. The number of occupied subbands N_c changes at the magnetic fields indicated by the vertical dotted lines.

square $W = L$. When the length is larger than $\sim 10l$, the fluctuation becomes smaller due to the localization effect.

A brief comment on effects of the evanescent states is worthwhile. The evanescent states correspond to virtual processes in scatterings. Therefore, by their inclusion the higher Born scatterings from a single impurity can automatically be taken into account. The major part of the effects noted in the papers [25, 26] is probably those of such higher Born scatterings. We have chosen $\tilde{\gamma}$ as small as possible (and assumed equal amounts of attractive and repulsive impurities) in order to reduce the higher Born effects. Consequently, the evanescent states have little influence on the conductance except when the Fermi level lies just below the bottom of an excited subband, where the subband broadening cannot otherwise be treated properly. In fact, the calculated conductance suffers little change even if the evanescent states are completely neglected, when the Fermi level lies in the middle of the bottoms of two adjacent subbands.

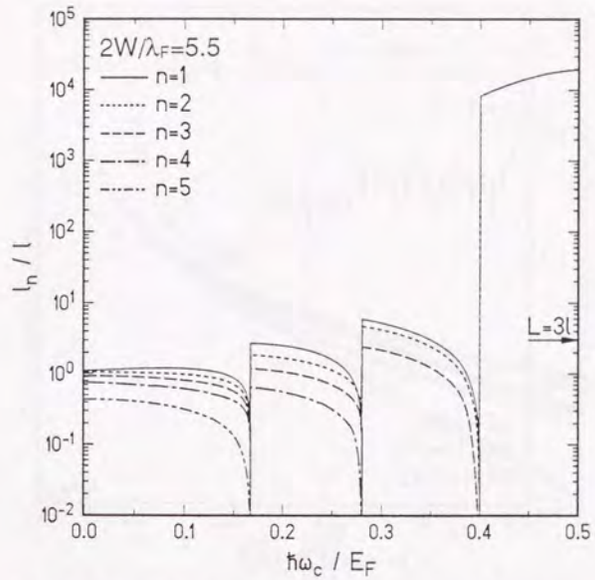

Fig. 11 Mean free path of each subband as a function of a magnetic field for the same system as that in Fig. 10. The mean free path exceeds the sample length when the occupied channel number becomes three.

C. Magnetic Field

An example of calculated conductance as a function of the magnetic field is shown in Fig. 10. We consider a system characterized by $2W/\lambda_F = 5.5$ and $l/\lambda_F = 51.25$ with fixed length $L = 3l$, where the fluctuation becomes nearly maximum in the absence of magnetic fields, and vary the magnetic field at a fixed value of the Fermi energy. In the presence of very weak magnetic fields ($\hbar\omega_c/E_F \lesssim 1 \times 10^{-2}$), the conductance increases slightly from the value at zero field probably due to a reduction in the weak localization effect. At higher magnetic fields, the conductance exhibits an oscillatory dependence on the field.

This behavior can be understood simply in terms of the magnetic-field dependence of the mean free path. The mean free path of each subband shown in Fig. 11 is calculated by solving the Boltzmann transport equation [76]. Whenever the Fermi level is close to a subband bottom, the mean free path decreases drastically due to the divergence in the 1D density of states. The decrease in the conductance at each subband bottom corresponds to this strong enhancement of scattering effects. Except at such

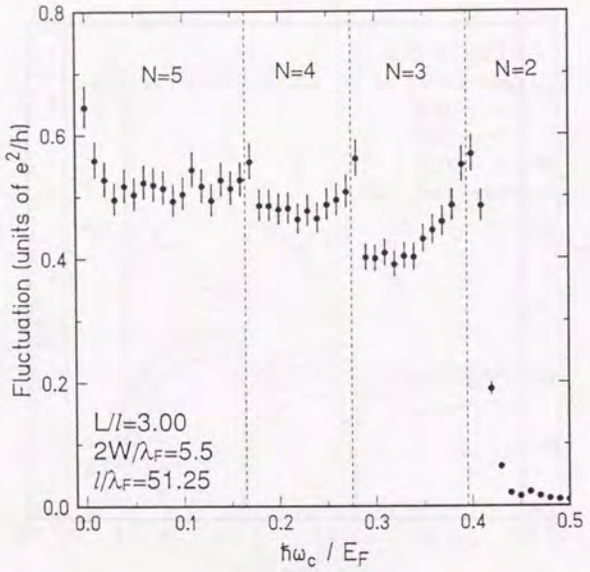

Fig. 12 The fluctuations as a function of the magnetic field for the same system as that in Fig. 10

magnetic fields the mean free path increases gradually with magnetic field. In magnetic fields, electrons are pushed toward the wire edges, the overlap between wavefunctions associated with positive and negative velocity becomes small, and backscattering rates are lowered. At the magnetic field ($\hbar\omega_c/E_F \approx 0.4$) where the channel number changes from 3 to 2, the mean free path increases by several orders of magnitude and exceeds the system length. Correspondingly, the conductance rapidly approaches the quantized value $G=2N_c(e^2/h)$. In such a strong field well-defined edge states are formed and the backscatterings between the edge states are completely suppressed. An electron in the edge states can move ballistically through the sample except when the energy is in the region of broadened bulk Landau levels where the edge states are strongly mixed with the bulk levels [77]. Edge states with a long mean free path in high magnetic fields have been the subject of both theoretical [55, 78] and experimental [79-81] investigations.

Figure 12 shows the corresponding result of the fluctuation. The reduction in the fluctuation which can be seen in weak magnetic fields ($\hbar\omega_c/E_F \lesssim 1\times10^{-2}$) corresponds to the suppression of the contribution from the so-called "particle-particle channel" predicted by perturbational calculations [6-10]. As a matter of fact, the flux penetrating

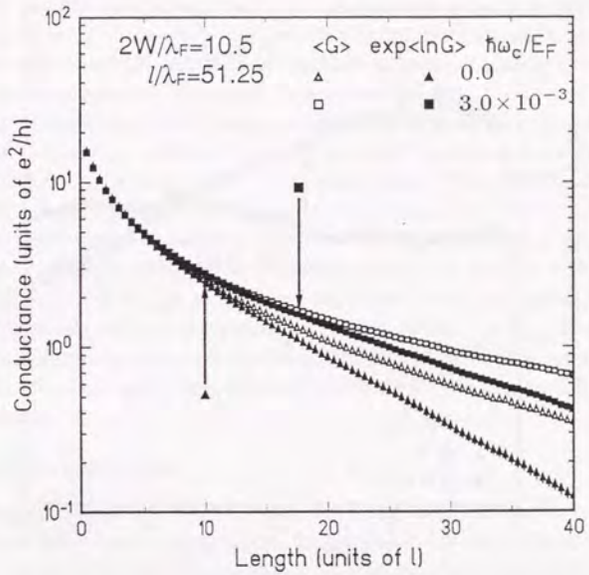

Fig. 13 Conductance as a function of the length L for $2W/\lambda_F = 5.5$ in the magnetic field corresponding to $\hbar\omega_c/E_F = 3\times10^{-3}$ compared with that at $B=0$. The magnetic flux penetrating through the area with length l and width W is $BlW = 2.5\times(h/e)$. The localization lengths are indicated by the vertical arrows.

through the sample is $BLW \sim 13\times(h/e)$ for $\hbar\omega_c/E_F \sim 1\times10^{-2}$. When the magnetic field is increased further, the fluctuation gradually decreases except in the vicinity of the fields where the subband depopulation occurs. This can be explained by the gradual approach of the system to the ballistic regime due to the increase in the mean free path. In strong magnetic fields ($\hbar\omega_c/E_F \gtrsim 0.45$) the fluctuation becomes negligibly small corresponding to the quantization of the conductance itself.

Figure 13 shows G as a function of L for $2W/\lambda_F = 10.5$ and $l/\lambda_F = 51.25$ in the weak field $\hbar\omega_c/E_F = 3\times10^{-3}$ together with G at $B=0$. In terms of the magnetic flux, each area normal to the field with length l and width W is penetrated by $BlW/(h/e) = 2.5$ flux. In the nearly ballistic regime ($L \ll l$), there is almost no difference between the conductances of $B=0$ and $B\neq0$, which is due to the fact that the mean free path is not affected by the weak magnetic field. As the length becomes larger, the conductance becomes larger than that at $B=0$ at every length. The localization length, denoted by

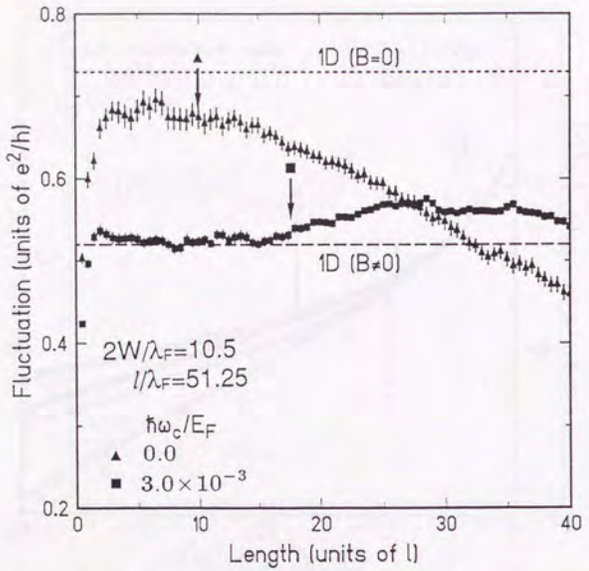

Fig. 14 Conductance fluctuations as a function of L in the presence of the magnetic field compared with those at $B=0$ for the same system as that in Fig. 13. The localization lengths are indicated by the vertical arrows. The universal values obtained by the perturbation calculation in quasi-one-dimensional wires are indicated by the horizontal dotted line ($B=0$) and the dashed line ($BLW \gg h/e$).

the vertical arrow, is 16.7 ± 0.6 in units of l, which is about 1.7 as large as that in the absence of a magnetic field.

In the limit of large channel numbers, it has been shown that ξ increases in proportion to βN_c in metallic wires, where the symmetry factor β is defined for a system of the orthogonal ($\beta = 1$), unitary ($\beta = 2$), and symplectic ($\beta = 4$) universality classes. Thouless [82] has assumed that the localization length roughly corresponds to the system length L where the conductance $ne^2\tau/mL$ becomes of the order of $e^2/\pi\hbar$. The same result has been derived analytically with the use of the supersymmetry method [83], the random-matrix method [84], and numerical calculations [85]. In the case of more general values of N_c, it has been shown by the previous calculation [86, 87], and it will be shown in Chapter 4, that the localization length ξ is given by $\xi \propto (\beta N_c + 2 - \beta)$. The present numerical result is in good agreement with this analytic expression which

shows that the localization length for $\beta = 2$ is 1.8 times as large as that for $\beta = 1$ in the case of $N_c = 10$. It should be noticed that, in contrast to metallic wires, quantum wires have well resolved 1D subbands and the actual value of ξ varies considerably as a function of the energy even for a given channel number [77].

Figure 14 shows the corresponding results for the fluctuation. The universal region can now be clearly seen as well as the reduction of δG in comparison with δG at $B=0$, when the sample is shorter than the localization length ($L < 15l$). The actual amount of the reduction is slightly smaller than that predicted by perturbational calculations ($\delta G(B)/\delta G(B=0) \simeq 0.8$ in contrast to $1/\sqrt{2} = 0.71$). This difference is to be expected because the mechanism leading to the reduction is absent in pure 1D wires with a single occupied subband. When the sample becomes longer than the localization length, δG somewhat increases, takes a maximum, and begins to decrease in the region $L > 35l$. The similar and even stronger enhancement of the fluctuation in this region occurs in the presence of spin-orbit interaction in Sec. 2.2 D where we will discuss this enhancement in more details.

D. Spin-Orbit Interaction

In treating spin-orbit scatterings and boundary roughness scatterings, it is more convenient to use a square-lattice model. In particular, effects of spin-orbit interaction can easily be introduced by the same model as that adopted in the study of symmetry effects on localization [88]. It is described by the Hamiltonian

$$H = \sum_i \varepsilon_i c_{i\sigma}^\dagger c_{i\sigma} - \sum_{i,j} V(i,\sigma;j,\sigma') c_{i\sigma}^\dagger c_{j\sigma'}, \tag{2.29}$$

where $V(i,\sigma;j,\sigma') = V_x$ or V_y depending on the direction of the nearest neighbor site in the x or y direction. In the matrix form we have

$$V_x = \begin{bmatrix} V_1 & V_2 \\ -V_2 & V_1 \end{bmatrix}, \quad V_y = \begin{bmatrix} V_1 & -iV_2 \\ -iV_2 & V_1 \end{bmatrix}, \tag{2.30}$$

with V_1 and V_2 being spin-diagonal and off-diagonal elements respectively and

$$|\uparrow\rangle = \begin{bmatrix} 1 \\ 0 \end{bmatrix}, \quad |\downarrow\rangle = \begin{bmatrix} 0 \\ 1 \end{bmatrix}. \tag{2.31}$$

This model of spin-orbit interaction with spin-splitting is different from the conventional one without spin-splitting used in metallic wires. However it is expected to simulate actual two-dimensional systems in n-channel inversion layers on surfaces of III-V semiconductors or at $GaAs/Al_xGa_{1-x}As$ heterostructures [88], and is enough in the study of the effect of symmetry on the conductance fluctuations.

Effects of scatterings from bulk impurities are introduced through randomness of site energy ε_i distributed uniformly with width $U(-U/2 \le \varepsilon_i + 4V \le U/2)$. This lattice

model corresponds to the wire containing high concentration of scatters with δ-function potentials, if we choose the parameters as

$$n_i\gamma^2 = a^2\left\langle(\varepsilon_i + 4V)^2\right\rangle = \frac{a^2U^2}{12}, \tag{2.32}$$

where n_i is the impurity density per area, γ is the strength of an impurity, and a is the lattice constant.

In a two-dimensional system without randomness ($\varepsilon_i = -4V$), the energy of an electron with wave vector $\mathbf{k} = (k_x, k_y)$ is given by an eigenvalue of the following 2×2 matrix

$$H(k) = \begin{bmatrix} 4V_1 - 2V_1(\cos k_x a + \cos k_y a) & -2V_2(i\sin k_x a + \sin k_y a) \\ -2V_2(-i\sin k_x a + \sin k_y a) & 4V_1 - 2V_1(\cos k_x a + \cos k_y a) \end{bmatrix}. \tag{2.33}$$

For small $k_x a$ and $k_y a$, Eq. (2.33) becomes

$$H(k) = \begin{bmatrix} \hbar^2k^2/2m & -2\hbar^2k_s(ik_x + k_y)/2m \\ -2\hbar^2k_s(-ik_x + k_y)/2m & \hbar^2k^2/2m \end{bmatrix}, \tag{2.34}$$

where

$$\frac{V_1}{E_F} = \frac{\hbar^2}{2ma^2E_F} = \left(\frac{1}{2\pi}\right)^2\left(\frac{\lambda_F}{a}\right)^2, \quad \frac{V_2}{E_F} = \frac{1}{2\pi}\frac{\lambda_F}{a}\frac{k_s}{k_F}. \tag{2.35}$$

The energy takes a minimum along the circle defined by $k = k_s$ instead of $k = 0$. We choose k_s/k_F as the parameter characterizing the strength of spin-orbit interaction. The presence of such a k-linear term was first pointed out by Ohkawa and Uemura [89] in n-channel inversion layers on narrow-band-gap $Hg_xCd_{1-x}Te$. It is quite difficult, however, to obtain a reliable estimate of the absolute magnitude of the k-linear term [50]. The randomness parameter is related to the mean free path l through

$$\frac{U}{E_F} = \left[\frac{6\lambda_F^3}{\pi^3a^2l}\right]^{1/2}. \tag{2.36}$$

We have checked that, in the absence of spin-orbit interaction, the results obtained by the lattice model are the same as those by the continuum model.

Figure 15 shows the calculated conductance as a function of sample length for $2W/\lambda_F = 5.25$ corresponding to the channel number 5. As is the same in the case of magnetic field, the initial decrease of the conductance in the nearly ballistic regime ($L \ll l$) does not depend on the strength of spin-orbit interaction, corresponding to the fact that the mean free path itself is not affected by the symmetry of the system. With further increase of the length, the conductance in the presence of spin-orbit interaction decreases more slowly than in its absence, which leads to the increase of the localization length by a factor of about 3. This result is in good agreement with the analytic expression in Chapter 4, $\alpha^{-1} \propto (\beta N_c + 2 - \beta)$, which shows that the localization length for $\beta = 4$ is three times as large as that for $\beta = 1$ in the case of $N_c = 5$.

The corresponding result for the fluctuation is given in Fig. 16. In the presence of spin-orbit interaction, the fluctuation is reduced by a factor close to 1/2 in the universal region ($l \ll L \ll \xi$). But with further increase of the length, it gradually becomes larger and takes a maximum around the length $\alpha^{-1} = 2\xi$, as is the same in the presence of a magnetic field (Sec. 2.2 C).

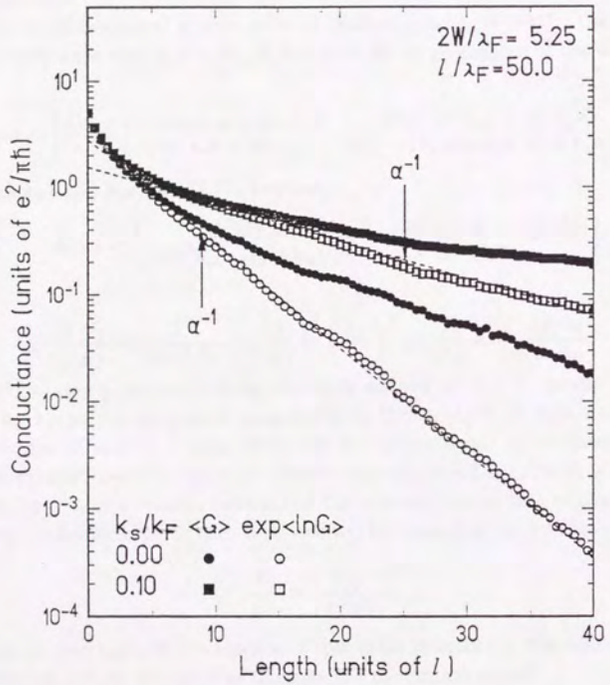

Fig. 15 Calculated conductance vs length in the presence (squares, $k_s/k_F = 0.1$) and the absence (circles) of spin-orbit interaction for wires with the channel number 5. Two different averages, arithmetic (filled symbols) and geometric (open symbols), are shown. The vertical arrows denote $\alpha^{-1} = 2\xi$ (ξ:the localization length). The dotted lines represent the straight lines corresponding to the localization lengths.

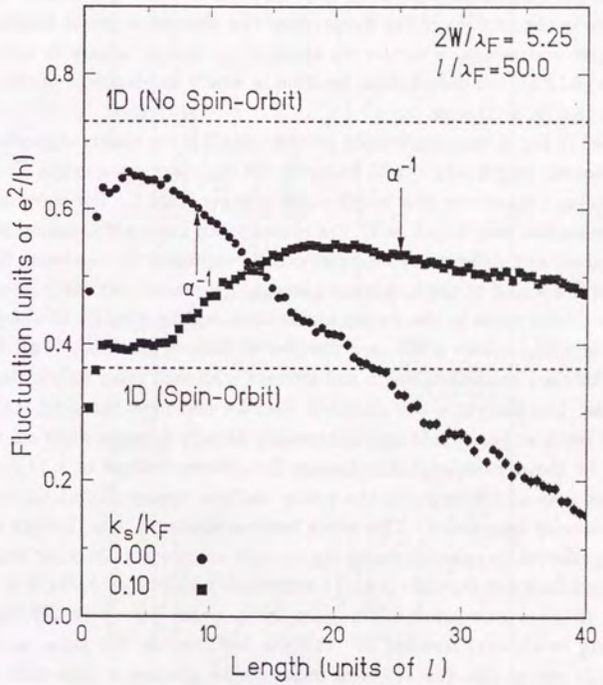

Fig. 16 Calculated fluctuation vs length in the presence (squares, $k_s/k_F = 0.1$) and the absence (circles) of spin-orbit interaction for wires with the channel number 5. The vertical arrows denote $\alpha^{-1} = 2\xi$ (ξ : the localization length). The horizontal dotted lines denote the fluctuations calculated perturbationally for metallic 1D wires.

To understand this length dependence more clearly, we look at the distribution function of the conductance. Figure 17 shows calculated distribution functions in the (a) presence and (b) absence of spin-orbit interaction, corresponding to lengths $\alpha L \sim 1/8, 1/4, 1/2, 1$, and 2. In the universal region, the conductance nearly obeys a normal Gaussian distribution around the mean value. The width of the distribution becomes narrower in the presence of spin-orbit interaction than its absence. The distribution function changes qualitatively when its left tail reaches the origin $G = 0$. Because of the difference in the amount of the fluctuation, this change occurs at lengths $\alpha L \lesssim 1/2$ with spin-orbit scatterings, while for its absence the change occurs at $\alpha L \lesssim 1/4$. For longer wires ($\alpha L \gtrsim 1$), the distribution function is nearly independent of the symmetry and close to that in a 1D wire.

As shown in Fig. 6, the distribution function in 1D wires clearly changes its feature around a crossover length $\alpha L_c \sim 1/2$, where its left tail reaches the origin. In Fig. 7, the fluctuation takes a maximum at a length slightly larger than L_c. For wires much longer than the localization length ($\alpha L \gg 1$), the conductance and its fluctuation for different channel-numbers and different symmetries can be expressed by the same functions of the length, if it is scaled by the localization length. This result can easily be understood because the conductance in the strong localization regime consists of sharp peaks at energies of localized states which are distributed almost randomly with broadening determined by the localization length and interact with each other only if their energies are very close. The analytical calculation in Sec. 4.4 also gives the same scaling result. The present result suggests that this universality already appears when $\alpha L \sim 1$.

Figure 18 shows calculated fluctuations for different values of k_s/k_F. The fluctuation takes a small maximum in the nearly ballistic regime ($1 \lesssim \alpha L \lesssim 2$) particularly for weak spin-orbit interaction. This arises because electrons pass through the system before being affected by spin-flip scattering for such short wires. In other length region, the fluctuation does not depend on k_s/k_F appreciably as long as $k_s/k_F \neq 0$.

Figure 19 gives calculated fluctuations for a wider wire with $2W/\lambda_F = 10.25$ corresponding to channel number 10. All the features are the same as those with $2W/\lambda_F = 5.25$ except that the universal region in the absence of spin-orbit interaction has become much clearer and the reduction due to the spin-orbit interaction has become further close to 1/2.

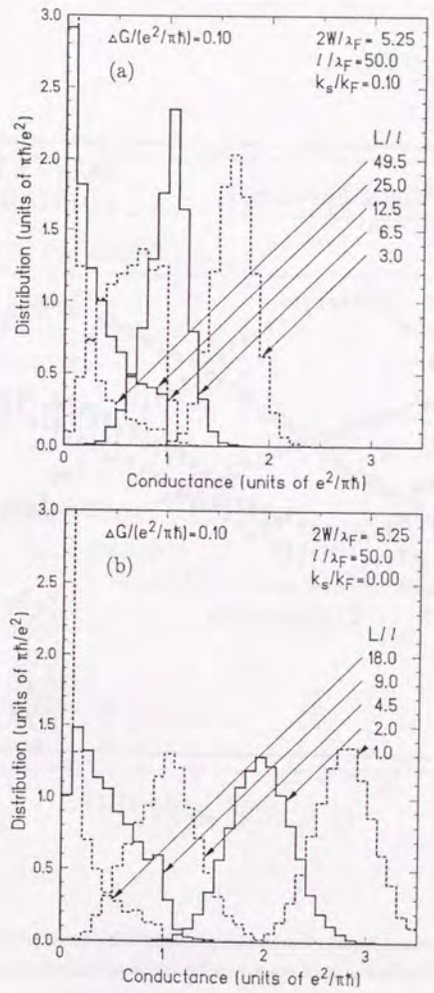

Fig. 17 Calculated histograms of the conductance in (a) the presence and (b) the absence of spin-orbit interaction. The length of the wire L chosen in such a way that $\alpha L \sim 2, 1, 1/2, 1/4$, and $1/8$ from the top.

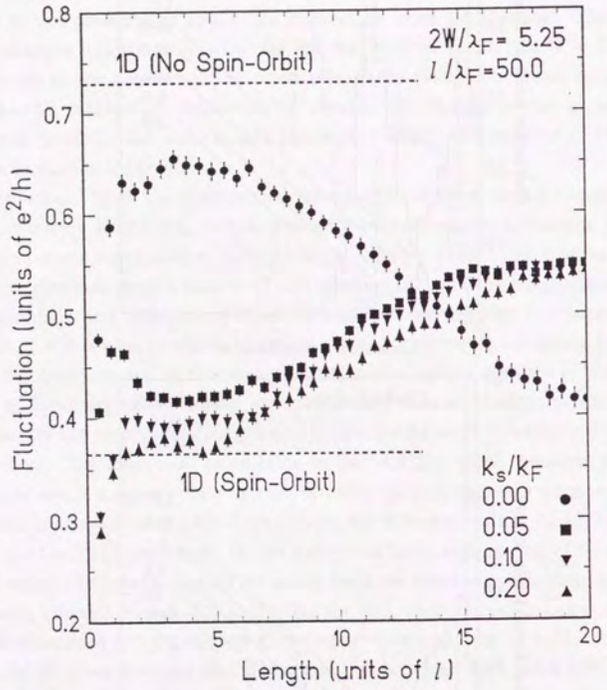

Fig. 18 Calculated conductance fluctuation vs length for several values of the spin-orbit parameter k_s/k_F. The horizontal lines denote the fluctuation calculated perturbationally for metallic 1D wires.

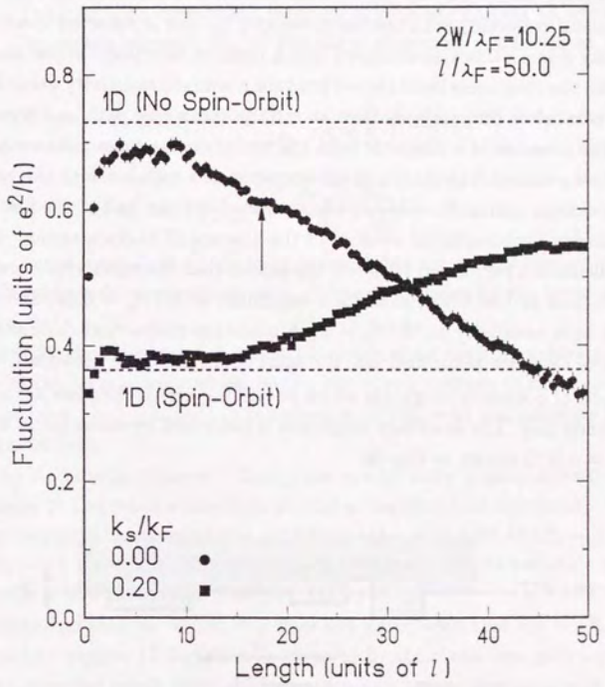

Fig. 19 Calculated conductance fluctuation vs length in the presence (squares) and the absence (circles) of spin-orbit interaction for wires with channel number 10. The vertical arrows denote $\alpha^{-1} = 2\xi$ (ξ : the localization length). The horizontal lines denote the fluctuation calculated perturbationally for metallic 1D wires.

E. Boundary Roughness Scattering

It was shown experimentally [90] that long quantum wires exhibited a large positive magnetoresistance due to the effect of boundary roughness scattering. A similar magnetoresistance has already been observed in aluminum films [91] and explained by a classical-trajectory model [92]. In the classical theory, it is assumed that each electron follows a classical trajectory with the Fermi velocity v_F and is reflected specularly with the probability p and otherwise scattered into a random direction. In the absence of a magnetic field, the roughness itself cannot produce a nonzero resistivity because straight trajectories parallel to film surfaces have an infinite mean free path and dominant the current. In the presence of a magnetic field, the resistivity becomes nonzero because all electrons follow a curved trajectory and are scattered at a collision with the boundaries. When the cyclotron radius $R_c = v_F/\omega_c$ becomes smaller than half of the film thickness W, the resistivity vanishes again because of the absence of backscattering. A detailed numerical calculation performed for $p = 0$ has shown that the resistivity increased with the magnetic field at low fields, exhibits a maximum at $W/R_c \approx 0.55$, and decreased down to the bulk resistivity at $W/R_c = 2$. A quantum-mechanical calculation [93] in quantum wires has been performed and the same result has been obtained.

The model of boundary roughness which we will use here is the same as that used by Akera and Ando [93]. The boundary roughness is described by deviation of boundaries $\Delta_{\pm}(x)$ at $y = \pm W/2$ shown in Fig. 20.

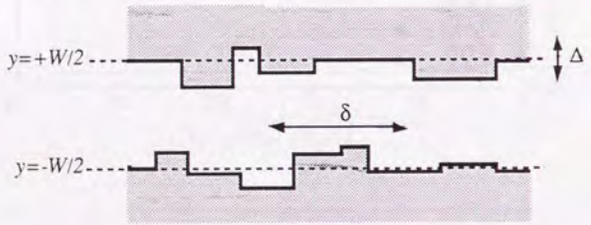

Fig. 20 The model of boundary roughness. δ is the correletion length, with which the next variation of the wall occurs. Δ is the average displacement or the root-mean-square deviation of the wall.

The wire is separated into narrow segments whose length takes nd_0 ($n = 1, 2, \cdots, n_\Delta$) with probability n_d^{-1}. Within each segment, the left and right boundaries are shifted by $\pm m\Delta_0 (m = 1, 2, \cdots, n_\Delta)$ with probability q/n_Δ and are left unshifted

with $1 - 2q$. This gives the correlation function of roughness $\Delta_+(x)$ of the left boundary and $\Delta_-(x)$ of the right boundary as

$$\langle \Delta_{\pm}(x)\Delta_{\pm}(x')\rangle = \sqrt{\pi}\delta\Delta^2 g(x - x'), \tag{2.37}$$

with correlation length $\delta = (2n_d + 1)d_0/3\sqrt{\pi}$ and average displacement $\Delta^2 = q(n_\Delta + 1)(2n_\Delta + 1)\Delta_0^2/3$. The correlation function $g(x)$ is normalized to unity and $g(0) = 1/\sqrt{\pi}\delta$. The matrix element $H'_{\pm}$ of boundary roughness scattering at $y = \pm W/2$ is given by

$$\langle n'k'|H'_{\pm}|nk\rangle = \frac{\hbar^2}{2m} Y^{\pm}_{n'k'nk} \frac{1}{L} \int dx \Delta_{\pm} e^{i(k-k')x}, \tag{2.38}$$

where

$$Y^{\pm}_{n'k'nk} = \mp \frac{\partial \psi_{n'k'}}{\partial y} \frac{\partial \psi_{nk}}{\partial y}\bigg|_{\pm W/2}, \tag{2.39}$$

where ψ_{nk} is the solution of Eq. (2.3). It is noted that the matrix element is proportional to the differential of the wavefunction $\psi_{nk}(y)$ and is smaller for the lower subbands since $|Y^{\pm}_{n'k'nk}| = 2\pi^2 n' n/W^3$.

Figure 21 shows calculated conductance for wires with boundary roughness as a function of the length, normalized by the arithmetic average of the mean free path of each subband ($l_A = \sum_n l_n/N$), in the absence ($W/R_c = 0$) and presence ($W/R_c = 0.5$) of a magnetic field.

In the Boltzmann transport theory, the conductivity is proportional to the l_A (see also Chapter 3) and takes a minimum around a magnetic field corresponding to $W/R_c = 0.5$. The reduction in the mean free path from $l/\lambda_F \sim 11.8$ for $W/R_c = 0$ to $l/\lambda_F \sim 4.6$ for $W/R_c = 0.5$ shows that the resistivity is enhanced from its zero-field value by more than double in the Boltzmann transport theory.

The conductance for $W/R_c = 0$ does not agree with that for $W/R_c = 0.5$ in the nearly ballistic regime ($L/l_A \lesssim 1$) even if scaled by the mean free path except at $L = 0$. This is an expected result because of the singularly strong dependence of the mean free path on 1D subbands. In the limit of short-range boundary roughness ($\delta/\lambda_F \ll 1$), the Boltzmann transport theory predicts that $\tau_n^{-1} \propto n^2$ for $W/R_c = 0$, where τ_n is the relaxation time of an electron in the subband n. Because of an extra n dependence due to the velocity v_n, the mean free path $l_n = v_n\tau_n$ exhibits even stronger dependence than n^{-2}. In fact, the actual calculation shows that for $2W/\lambda_F = 5.25$ the mean free path of the lowest subband is about two orders of magnitude larger than that of the highest subband. The decrease in the nearly ballistic region is likely to be determined by the harmonic average of l_n, $l_H^{-1} = \sum_n l_n^{-1}/N$, which is much smaller than l_A.

Figure 22 shows that corresponding fluctuation as a function of length. The fluctuation takes a sharp maximum in the nearly ballistic region ($L/l_A \lesssim 1$) and starts to

decrease around the localization length both in the absence and the presence of a magnetic field. There is no universal region where the fluctuation remains independent of L because the wire is still too narrow.

Figures 23 and 24 give the result for a wider wire with channel number 10 ($2W/\lambda_F = 10.25$). The magnetic-field reduction in the mean free path is much larger than that for $2W/\lambda_F = 5.25$. The universal region appears in the region $l \ll L \ll \alpha^{-1}$, where the fluctuation in the absence of a magnetic field is clearly smaller than that of 1D metallic wires. The singular enhancement of the fluctuation in the nearly ballistic region is stronger than that in narrower wires.

In short wires, mixing among different 1D subbands due to scattering is not appreciable and each channel may be regarded as almost independent. The transmission probability of the low-lying subbands has a sharper distribution with peak close to unity because of the large mean free path, while that of the higher subbands has a broader distribution with peak at much smaller than unity. This is presumably a main origin of the singular enhancement of the fluctuation in the near-ballistic regime. This enhancement may be related to the suggestion by Higurashi, Iwabuchi, and Nagaoka [94], who claimed that the fluctuation can be enhanced considerably in the near-ballistic regime even for bulk impurity scattering within a lattice model containing a peculiar anisotropy. In our model, which simulates actual quantum wires much better, however, such enhancement has not been obtained for bulk scatterers.

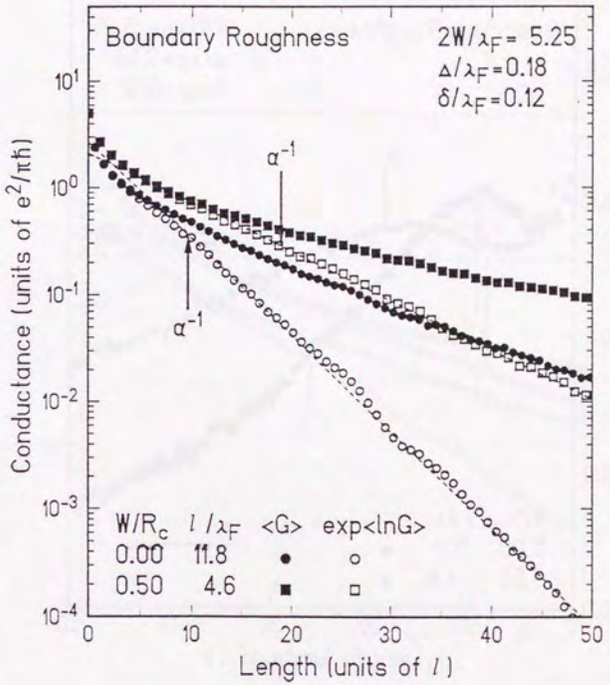

Fig. 21 Calculated conductance due to boundary roughness scattering vs length in the presence (squares) and the absence (circles) of a magnetic field for wires with channel number 5. The correlation length $\delta/\lambda_F \sim 0.12$ and the mean deviation $\Delta/\lambda_F \sim 0.18$. Two different averages, arithmetic (filled symbols) and geometric (open symbols) are shown. The vertical arrows denote $\alpha^{-1} = 2\xi$. The horizontal dotted lines represent the fluctuations calculated perturbationally for metallic wires.

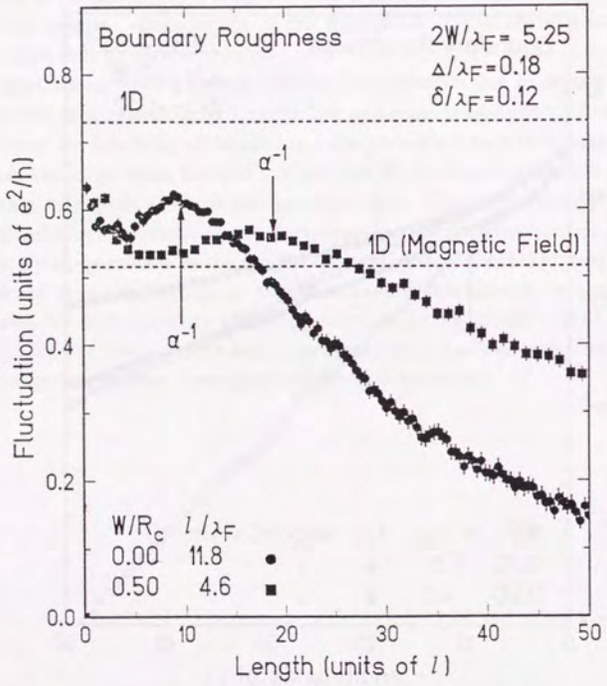

Fig. 22 Calculated fluctuation due to boundary roughness scattering vs length in the presence (squares) and the absence (circles) of a magnetic field for wires with channel number 5. The vertical arrows denote $\alpha^{-1} = 2\xi$ (ξ : the localization length). The horizontal dotted lines represent the fluctuations calculated perturbationally for metallic wires.

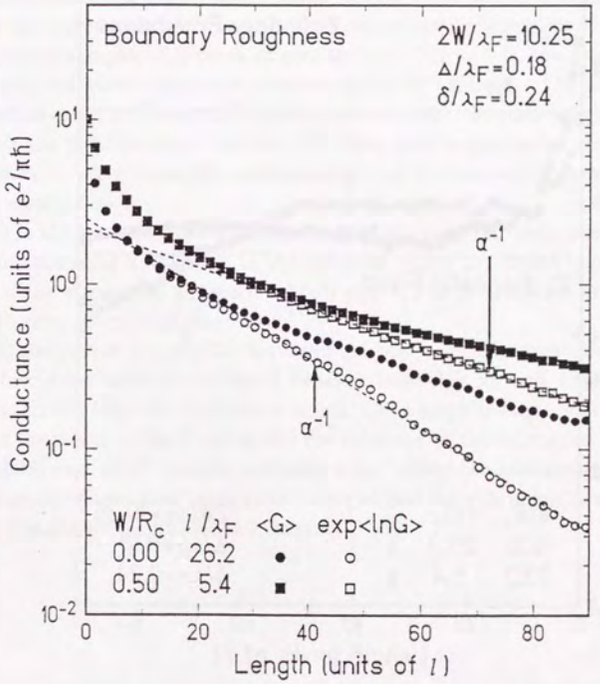

Fig. 23 Calculated conductance due to boundary roughness scattering vs length in the presence (squares) and the absence (circles) of a magnetic field for wide wires with channel number 10. The correlation length $\delta/\lambda_F \sim 0.24$ and the mean deviation $\Delta/\lambda_F \sim 0.18$. The dotted lines represent the straight lines corresponding to $\alpha^{-1} = 2\xi$.

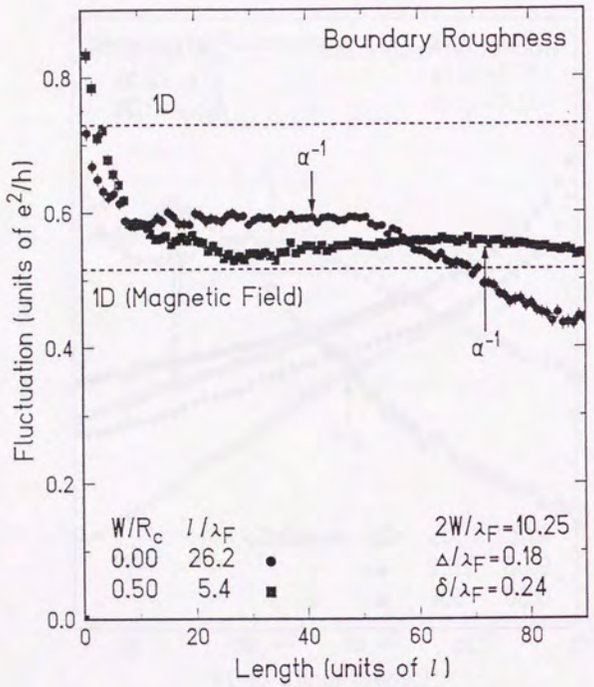

Fig. 24 Calculated fluctuation due to boundary roughness scattering vs length in the presence (squares) and the absence (circles) of a magnetic field for wide wires with channel number 10.

2.3 Summary

In conclusion, we have numerically studied electrical transport, especially conductance fluctuations and localization, in quantum wires in the presence of magnetic fields, spin-orbit interaction, and boundary roughness. The important results are summarized as follows.

(i) When only a few subbands are occupied in the absence of magnetic field and spin-orbit interaction and in the presence of bulk impurities, ξ is comparable to l and there is no universal region where the fluctuations stay independent of L. When many subbands are occupied, ξ is much longer than l ($\xi \sim N_c l$ with N_c the number of occupied subbands) and there appears a universal region in $l \lesssim L \lesssim \xi$. The absolute value of the fluctuation in the universal region is close to that obtained for quasi-1D metallic wires by the perturbational method. We have also demonstrated that the crossover from quantum wires to metallic wires occurs when the broadening exceeds the subband energy separations.

(ii) In the presence of a weak magnetic field or spin-orbit interaction, the amplitude of the conductance fluctuation in the universal region is reduced and the reduction-factor of the fluctuation approaches $1/\sqrt{2}$ and $1/2$ in the presence of magnetic fields and spin-orbit interaction respectively.

(iii) Because of the peculiar nature of boundary-roughness scattering, the conductance fluctuation exhibits a different behavior from that for bulk impurities when the length is shorter than the localization length, *i.e.*, a singular enhancement of the fluctuation in the nearly ballistic region and the reduction of the fluctuation in the universal region from that of 1D metallic diffusive wires. When the localization effect becomes important, the fluctuation becomes the same as that for bulk impurity scattering, if the length is scaled by the localization length.

Chapter 3

Perturbational Study of Mesoscopic Transport

In the previous numerical calculation, there remained the question whether the amplitude of conductance fluctuations in the universal region is the same as that in metallic wires. In this chapter, we study electrical transport in quantum wires by the conventional diagrammatic perturbational technique and calculate the amplitude of fluctuations, as well as the conductivity itself and the weak-localization correction, in order to answer this question.

Fukuyama [95] studied the weak localization in the presence of intervally scatterings in Si-MOS by use of the perturbational method. In the study of intersubband scattering by the perturbational method, Cantrell and Butcher [96] and Kearney and Butcher [97] studied the Boltzmann transport and the weak localization in quasi-two-dimensional (Q2D) and quasi-one-dimensional (Q1D) systems respectively. The weak localization and conductance fluctuation in Q2D systems were calculated by Iwabuchi and Nagaoka [98], and the weak localization in Q1D wires (*i.e.*, quantum wires) was studied by Suhrke *et al.* [99]. Iwabuchi and Nagaoka have shown that the amplitude of the conductance fluctuations in quasi-2D systems is exactly the same as that in 2D films in the limit of strong intersubband scatterings at $T = 0$.

In Sec. 3.1, we describe the model of calculation and obtain the one-particle Green function in quantum wires. We calculate the Boltzmann conductivity (Sec. 3.2), the weak localization correction (Sec. 3.3), and the conductance fluctuation (Sec. 3.4). Finally we give a summary in Sec. 3.5.

3.1 Model

The Hamiltonian is given by Eq. (2.1), except that we consider the system in the absence of magnetic fields $B = 0$. Using the normalized eigenfunction $\xi_{nk}(x,y) = L^{-1/2}e^{ikx}\psi_n(y)$ without impurities, the scattering part in the Hamiltonian (2.1) is expressed in the second-quantized form as

$$\begin{aligned} H' &= \sum_{n,n',k,q} V_{nn'}(q) c^\dagger_{n'k-q} c_{nk} \\ V_{nn'}(q) &= \frac{1}{L}\int dy \psi^*_{n'}(y) \left(\sum_{i=1}^{N_I} \gamma e^{-iqx_i} \delta(y-y_i) \right) \psi_n(y). \end{aligned} \tag{3.1}$$

The one-particle retarded and advanced Green function satisfy the Dyson equation

$$\begin{aligned} \left\langle G^\pm_{nn'}(k,\omega) \right\rangle &= G^0_n(k,\omega)\delta_{nn'} + \sum_{n_1} \left\langle G^\pm_{nn_1}(k,\omega) \right\rangle \left\langle \Sigma^\pm_{n_1n'}(k,\omega) \right\rangle G^0_{n'}(k,\omega), \\ G^0_n(k,\omega) &= \left[\hbar\omega - E_n - \hbar^2k^2/2m \right]^{-1}, \end{aligned} \tag{3.2}$$

where $\langle \cdots \rangle$ denotes the averaging over impurity configurations and $E_n = (\hbar^2/2m)(\pi n/W)^2$. In the matrix form, this Dyson equation is expressed as

$$\left\langle G^\pm(k,\omega) \right\rangle^{-1} = G^0(k,\omega)^{-1} - \left\langle \Sigma^\pm(k,\omega) \right\rangle. \tag{3.3}$$

We assume that the energy broadenings due to disorder are smaller than the separations between adjacent subband bottoms in quantum wires and that the Fermi level is well away from the broadened subband bottoms, *i.e.*,

$$|E_F - E_n|, |E_n - E_{n'}| \gg \left| \left\langle \Sigma^\pm_{n''n'''}(k,\omega) \right\rangle \right|. \tag{3.4}$$

Under this condition, the perturbed Green function (3.3) can be approximated by diagonal matrix and Eq. (3.2) is given by

$$\left\langle G^\pm_n(k,\omega) \right\rangle = G^0_n(k,\omega) + \left\langle G^\pm_n(k,\omega) \right\rangle \left\langle \Sigma^\pm_{nn}(k,\omega) \right\rangle G^0_n(k,\omega), \tag{3.5}$$

where we used a single subscript n for the diagonal Green function. The diagonal self-energy is calculated in the Born approximation by

$$\left\langle \Sigma^\pm_{nn}(k,\omega) \right\rangle = \sum_{n_1,q} \frac{\langle V_{nn_1}(q) V_{n_1n}(-q) \rangle}{\hbar\omega - E_{n_1} - \hbar^2(k-q)^2/2m \pm i\Gamma_{n_1}}, \tag{3.6}$$

and the perturbed one-particle Green function is given by

$$\left\langle G^\pm_n(k,\omega) \right\rangle = \left[\hbar\omega - E_n - \hbar^2k^2/2m \pm i\Gamma_n \right]^{-1}, \tag{3.7}$$

where $-\Gamma_n$ is the imaginary part of the self-energy Σ^+_{nn} and $\langle V_{nn_1}(q)V_{n_1n}(-q)\rangle$ is given by

$$\langle V_{nn_1}(q) V_{n_1n}(-q) \rangle = \frac{n_i\gamma^2}{L} \int dy \left|\psi_n(y)\right|^2 \left|\psi_{n_1}(y)\right|^2 \equiv \frac{1}{L}\Phi_{nn_1}. \tag{3.8}$$

By taking the imaginary part of Eq. (3.6) and changing the q summation into integral by $\sum_q \to (L/2\pi)\int dq$, we obtain Γ_n as

$$\begin{aligned}\Gamma_n &= -\mathrm{Im}\left\langle \Sigma_n^+(k,\omega)\right\rangle = \sum_{n_1}\int \frac{dq}{2\pi}\Phi_{nn_1}\frac{\Gamma_{n_1}}{\left[\hbar^2q^2/2m+E_{n_1}-E_F\right]^2+\Gamma_{n_1}^2} \\ &= \sum_{n_1}\frac{\Phi_{nn_1}}{2\hbar}\sqrt{\frac{2m\left(E_F-E_{n_1}\right)}{\left(E_F-E_{n_1}\right)^2+\Gamma_{n_1}^2}} \cong \sum_{n_1}\frac{\Phi_{nn_1}}{\hbar v_{n_1}^F},\end{aligned} \tag{3.9}$$

where we defined the velocity of an electron at the Fermi energy in the channel n by $v_n^F \equiv [2(E_F-E_n)/m]^{1/2}$ and used Eq. (3.4).

3.2 Boltzmann Conductivity

Unaveraged conductivity is given by

$$\begin{aligned}\sigma = \frac{\pi\hbar^3e^2}{m^2L}\sum_{n,n',k,k'}\frac{kk'}{(2\pi i)^2}&\left(G_{nn'}^+(k,k',E_F)-G_{nn'}^-(k,k',E_F)\right) \\ &\times\left(G_{n'n}^+(k',k,E_F)-G_{n'n}^-(k',k,E_F)\right),\end{aligned} \tag{3.10}$$

where $G_{nn'}^{\pm}(k,k',E_F)$ is the unaveraged Green function propagating from state (n,k) to (n',k'). When Eq. (3.10) is averaged over impurity configurations, the most dominant contribution in the large channel limit $N = N_c \gg 1$ comes from the so-called ladder diagram schematically shown in Fig. 25.

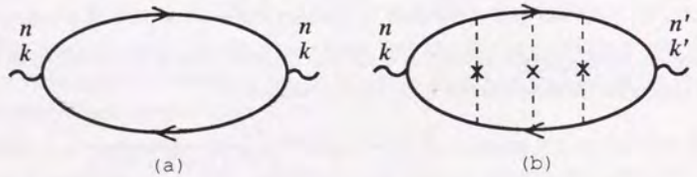

Fig. 25 Diagrams that should be considered for conductivity. Dashed line with a crossed symbol denotes the scattering from an impurity.

As is usual in the case of scattering by impurity potential of δ-function type in the absence of magnetic fields, the contribution from the diagram with a ladder (b) vanishes and only the diagram (a) gives non-zero contribution. Then the Boltzmann

conductivity is given by

$$\begin{aligned}\sigma^B &= \frac{\hbar e^2}{2\pi m^2L}\sum_{n,k}\frac{k^2}{\left(E_F-E_n-\hbar^2k^2/2m\right)^2+\Gamma_n^2} = \frac{e^2}{2\pi\hbar^2m^2L}\sum_n\frac{L}{2\pi}\frac{2\pi mk_n^F}{\Gamma_n} \\ &= \frac{e^2}{h}\sum_n l_n \equiv \frac{e^2}{h}Nl,\end{aligned} \tag{3.11}$$

where $k_n^F = mv_n^F/\hbar$. The mean free path l_n for the subband n is defined by

$$l_n^{-1} \equiv \frac{\Gamma_n}{v_n^F} = \sum_{n'=1}^{N}\frac{\Phi_{nn'}}{\hbar^2v_n^Fv_{n'}^F}. \tag{3.12}$$

As seen from Eq. (3.11), the Boltzmann conductivity σ^B for quantum wires is expressed in terms of the arithmetic mean of l_n. This result is in agreement with the result of the semiclassical Boltzmann transport theory [93].

3.3 Weak Localization Correction

Before we calculate the correction to the Boltzmann conductivity, we show the general feature of the ladder diagrams in quantum wires. General (cooperon) ladder diagram is given in Fig. 26, where the subband indices of a pair of the upper- and lower-propagators between two adjacent scatterings are not necessarily the same.

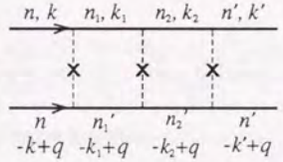

Fig. 26 Ladder diagram.

In the intermediate part of the ladder in Fig. 26, there appears a term like

$$I_{n_1n_1'} \equiv \sum_q \left\langle V_{nn_1}(k-k_1)V_{n_1'n}(k_1-k)\right\rangle\left\langle G_{n_1}^+(k_1,\omega)\right\rangle\left\langle G_{n_1'}^-(-k_1+q,\omega)\right\rangle. \tag{3.13}$$

By calculating Eq. (3.13), we can show that

$$I_{n_1\neq n_1'}/I_{n_1n_1} \sim \Gamma_{n_1}/\left|E_{n_1}-E_{n_1'}\right| \ll 1, \tag{3.14}$$

where we have used the condition Eq. (3.4). Therefore we only have to consider the

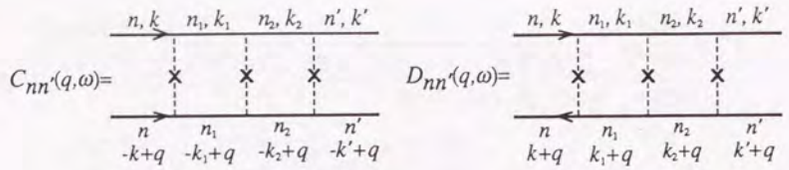

Fig. 27 Cooperon ladder and diffuson ladder.

ladder diagrams in which the subband index of a pair of the upper- and the lower-propagators is the same. From this fact, the cooperon ladder and diffuson ladder to be considered are shown schematically in the Fig. 27.

The cooperon ladder satisfies the following equation

$$C_{nn'}(q) = \frac{\Phi_{nn'}}{L} + \sum_{n_1,k_1} \frac{\Phi_{nn_1}}{L} \left\langle G^+_{n_1}(k_1,\omega)\right\rangle \left\langle G^-_{n_1}(-k_1+q,\omega)\right\rangle C_{n_1n'}(q). \tag{3.15}$$

For a small q, we obtain

$$\sum_{k_1} G^+_{n_1}(k_1,\omega) G^-_{n_1}(-k_1+q,\omega) = \frac{L}{\hbar v^F_{n_1}\Gamma_{n_1}} \left(1 - \left(\frac{\hbar v^F_{n_1}}{2\Gamma_{n_1}}\right)^2 q^2\right). \tag{3.16}$$

Substituting Eq. (3.16) into Eq. (3.15) and solving the equation for a small q, we obtain the cooperon as

$$C_{nn'}(q) = \frac{4\Gamma_n\Gamma_{n'}}{L}\left(\sum_m \frac{\hbar v^F_m}{\Gamma_m} q^2\right)^{-1} = \frac{4\Gamma_n\Gamma_{n'}}{2\pi\hbar N(0)L}(Dq^2)^{-1}, \tag{3.17}$$

where $N(0) = \sum_m (1/\pi\hbar v^F_m)$ is the total density of states (per spin) at the Fermi energy and the diffusion constant D is defined by

$$D \equiv \frac{1}{2\pi N(0)} \sum_{m=1}^{N} \frac{v^F_m}{\Gamma_m}. \tag{3.18}$$

Diffuson $D_{nn'}(q)$ is obtained in the similar calculation as $D_{nn'}(q) = C_{nn'}(q)$.

Correction to the Boltzmann conductivity is calculated with the so-called maximal crossed diagram as shown in Fig. 28. The weak localization correction is given by

$$\begin{aligned}\sigma^{WL} = \frac{\hbar^3 e^2}{2\pi m^2 L} \sum_{n,n',k,q} & k(-k+q) \\ & \times \left\langle G^+_n(k)\right\rangle \left\langle G^-_n(k)\right\rangle \left\langle G^+_{n'}(-k+q)\right\rangle \left\langle G^-_{n'}(-k+q)\right\rangle \tilde{C}_{nn'}(q),\end{aligned} \tag{3.19}$$

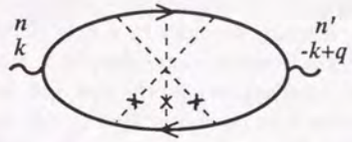

Fig. 28 Maximal crossed diagram giving a weak localization correction to the Boltzmann conductivity.

where it is noted that $\tilde{C}_{nn'}(q)$, in which one propagator goes from the subband n to n' and another from n' to n, is different from $C_{nn'}(q)$, in which both go from n to n'. However by obtaining

$$L^{-1}\sum_k k^2 \left\langle G^+_n(k)\right\rangle \left\langle G^-_n(k)\right\rangle \left\langle G^+_{n'}(-k+q)\right\rangle \left\langle G^-_{n'}(-k+q)\right\rangle = \frac{mk^F_n}{2\Gamma^3_n}\delta_{nn'}, \tag{3.20}$$

and noting $\tilde{C}_{nn}(q) = C_{nn}(q)$, we can calculate the weak localization correction as

$$\begin{aligned}\sigma^{WL} &= \frac{-\hbar^3 e^2}{2\pi m^2} \sum_{n,q} \frac{mk^F_n}{2\hbar^2\Gamma^3_n} C_{nn}(q) = -\frac{e^2}{2\pi^2\hbar DN(0)L} \sum_{n,q} \frac{v^F_n}{\Gamma_n}\frac{1}{q^2} \\ &= -\frac{e^2}{\pi\hbar L}\sum_q \frac{1}{q^2} = -\frac{e^2 L}{h} \times \frac{1}{3}.\end{aligned} \tag{3.21}$$

In the numerical result in Fig. 10, we obtained $g^{WL} = \sigma^{WL}/L \simeq 0.15$ (per spin), which is smaller than 1/3 of Eq. (3.21). This is because the sample length and the channel number in the numerical calculation are not so large ($L/l = 3, N = 5$) where the perturbation is not good approximation.

3.4 Conductance Fluctuation

When we define the dimensionless conductance $g \equiv G/(e^2/h)$, the amplitude of conductance fluctuations δg is calculated by the square-root of the variance of conductance, *i.e.*, $F \equiv (\delta g)^2 = \langle g^2\rangle - \langle g\rangle^2$. The diagrams for conductance fluctuation are represented by the product of two conductivity bubbles connected each other by two diffusons (or two cooperons) as shown in Fig. 29 in the momentum representation [6-11]. The contribution from Fig. 29(a) is calculated as

$$F_a = \frac{1}{4(mL)^4}\sum_{n_1,n_2}(m^2L)^2 \frac{v^F_{n_1}v^F_{n_2}}{4(\Gamma_{n_1}\Gamma_{n_2})^3}\frac{(4\Gamma_{n_1}\Gamma_{n_2})^2}{(2\pi DN(0)L)^2}\sum_q \frac{1}{q^4} = \frac{1}{\pi^4}\sum_{m=1}\frac{1}{m^4} = \frac{1}{90}. \tag{3.22}$$

where $q = \pi m/L$ from the boundary condition for the diffusion propagator [6-11]. As seen from Eq. (3.22), subband-dependent parameters such as v_n^F and Γ_n are collected together into a subband-independent parameter $DN(0)$ and cancel when they are summed over the subband index. Similarly we obtain $F_a = F_b = -2F_c = -2F_d = 4F_e$. When we count spin factor by 2^2, the cooperon contribution by 2, the exchange of the retarded and the advanced Green functions between the inner and outer bubbles by 2, and the way of inserting vertices by 2 for (a) and by 4 for (b)-(e), the total value is $F = 8/15$ or $\delta g = \sqrt{8/15} = 0.730$. Then we conclude that the amplitude of the conductance fluctuation is universal also in quantum wires and the universal value is exactly the same as that in metallic wires.

In the presence of the boundary roughness scattering, as seen in Fig. 24, the amplitude of the conductance fluctuation in the universal region $l \ll L \ll \xi$ is smaller than 0.730 in the absence of magnetic fields. This is presumably because the mean free path in the highest subband is extremely small (about two orders of magnitude smaller than that of the lowest subband), and the perturbational treatment fails.

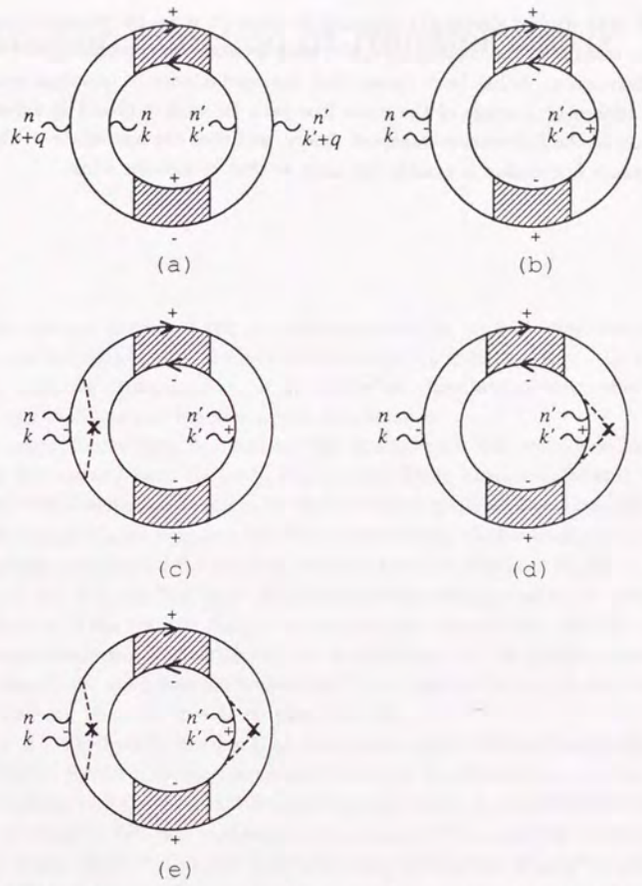

Fig. 29 Contributing diagrams to conductance fluctuations. Two shaded parts in a diagram is both cooperons or both diffusons, and the dashed line with a crossed symbol denotes the scattering by a single impurity.

3.5 Summary

We have studied electrical transports in quantum wires by perturbational method. We have calculated the conductance, the weak localization correction, and the conductance fluctuation. It has been shown that the conductance of quantum wires is given by the arithmetic average of the mean free path for each subband in agreement with the result of the Boltzmann transport theory, and that the amplitude of the universal conductance fluctuation is exactly the same as that in metallic wires.

Chapter 4
Distribution Function of Transfer Matrix

In the previous numerical and perturbational studies, we have calculated the conductance, its fluctuation, and the localization length in quantum wires, by averaging them over impurity configurations. If we obtain the distribution function of conductance, we can calculate any function of the conductance.

The exact distribution function of the conductance for 1D wires derived by Abrikosov has already been shown in Eq. (2.28). There have been several attempts to calculate the distribution function for multi-channel systems. Dorokhov [86] has obtained the Fokker-Planck equation for N one-dimensional chains weakly coupled with their neighbors and studied the localization of an electron. Mello *et al* [13, 15, 100, 101] and Pichard *et al* [87, 102, 103] have used the maximum entropy method in determining the distribution of the transfer matrix in the quasi-one-dimensional metallic wires and studied conductance and its fluctuation, and the localization. For quantum wires where the one-dimensional subbands are well-defined, it is possible to extend the method of Dorokhov, as will be shown in this chapter [104, 105].

In Sec. 4.1, we describe the model and derivation of the Fokker-Planck equation for the distribution function in quantum wires. In Sec. 4.2, the conductance, the conductance fluctuation, and the localization length are calculated by use of the Fokker-Planck equation obtained in Sec. 4.1. In Sec. 4.3, we compare the calculated results with the numerical results shown in Chapter 2 and give some discussions. Finally we give a brief summary in Sec. 4.4.

4.1 Differential Equation of Distribution Function

We extend an analytical method used by Dorokhov [86] to derive a Fokker-Planck equation of the distribution function of the conductance in quantum wires. We consider the same system as that in Chapters 2 and 3. The symmetry factor β is defined for a system without ($\beta = 1$) or with ($\beta = 2$) magnetic fields or with strong spin-orbit scattering ($\beta = 4$).

First we define a transfer matrix T for the disordered region as

$$\begin{bmatrix} O' \\ I' \end{bmatrix} = T \begin{bmatrix} I \\ O \end{bmatrix}, \tag{4.1}$$

where I, I' and O, O' are incoming and outgoing fluxes. The transfer matrix can be parametrized as [86, 106]

$$T = \begin{bmatrix} u & 0 \\ 0 & v \end{bmatrix} \begin{bmatrix} \cosh(\Gamma/2) & \sinh(\Gamma/2) \\ \sinh(\Gamma/2) & \cosh(\Gamma/2) \end{bmatrix} \begin{bmatrix} x & 0 \\ 0 & y \end{bmatrix}, \tag{4.2}$$

where Γ is an $N \times N$ ($2N \times 2N$) real diagonal matrix and u, v, x, and y are all $N \times N$ ($2N \times 2N$) unitary matrices for $\beta = 1$ and 2 (for $\beta = 4$). In case of $\beta = 1$, $v = u^*$ and $y = x^*$, and in case of $\beta = 4$, $v = \kappa u^* \kappa^T$ and $y = \kappa x^* \kappa^T$ where κ is defined by

$$\kappa = \begin{bmatrix} -i\sigma_y & & 0 \\ & \ddots & \\ 0 & & -i\sigma_y \end{bmatrix}, \quad -i\sigma_y = \begin{bmatrix} 0 & -1 \\ 1 & 0 \end{bmatrix}, \tag{4.3}$$

and $2N \times 2N$ matrix Γ for $\beta = 4$ has diagonal elements in pairs $\Gamma_1, \Gamma_1, \Gamma_2, \Gamma_2, \cdots, \Gamma_N, \Gamma_N$ and κ^T is the transposed matrix of κ.

Under this parametrization, the transmission matrix t and the two-terminal, multichannel version [53-57] of the Landauer formula [58] can be expressed as

$$t = u \frac{1}{\cosh(\Gamma/2)} x, \quad G = \frac{e^2}{h} \mathrm{Tr}\left(tt^\dagger\right) = \frac{e^2}{h} \mathrm{Tr}\left(\frac{2}{1+\cosh\Gamma}\right). \tag{4.4}$$

As seen from Eq. (4.4), the conductance is determined only by the parameter Γ.

It is very difficult to derive a Fokker-Planck differential equation for the distribution function, because the transfer matrix contains too many parameters and the differential equations become a set of complicated coupled equations of these parameters. Therefore we make two assumptions: (A) $\Gamma, u, x(, v, y)$ are statistically independent of each other and the distribution function is given by $W(L; \Gamma, u, v, x, y) = W(L; \Gamma) W(L; u) W(L; v) W(L; x) W(L; y)$. (B) All unitary matrices $u, x(, v, y)$ are equally probable, *i.e.*, are distributed according to the invariant measure of the unitary group [107], with which the second and fourth moments of elements of $N \times N$ unitary matrix u are given by

$$\begin{aligned} \left\langle u_{jk} u^*_{j'k'} \right\rangle_U &= N^{-1} \delta_{jj'} \delta_{kk'}, \\ \left\langle u_{jk} u_{lm} u^*_{j'k'} u^*_{l'm'} \right\rangle_U &= (N^2-1)^{-1} (\delta_{jj'} \delta_{ll'} \delta_{kk'} \delta_{mm'} + \delta_{jl'} \delta_{lj'} \delta_{km'} \delta_{mk'}) \\ &\quad - N^{-1} (N^2-1)^{-1} (\delta_{jj'} \delta_{ll'} \delta_{km'} \delta_{mk'} + \delta_{jl'} \delta_{lj'} \delta_{kk'} \delta_{mm'}), \end{aligned} \tag{4.5}$$

where $\langle \cdots \rangle_U = \int du \cdots$ denotes the average with the invariant measure of the unitary group $U(N)$. The validity of these assumptions will be discussed later.

Under these two assumptions, the expectation value of an arbitrary function of $\Gamma, \mathbf{U} = \{u, x(, v, y)\}$ is defined in terms of the distribution function $W(L; \Gamma, \mathbf{U}) = W(L; \Gamma) W(\mathbf{U})$ for the sample length L by

$$\langle F(\Gamma, \mathbf{U}) \rangle_L \equiv \int d\Gamma d\mathbf{U}\, F(\Gamma, \mathbf{U}) W(L; \Gamma, \mathbf{U}) = \int d\Gamma \, \langle F(\Gamma, \mathbf{U}) \rangle_U W(L; \Gamma). \tag{4.6}$$

Expanding $\langle F(\Gamma) \rangle_{L+\Delta L} = \langle F(\Gamma + \Delta\Gamma) \rangle_L$ with respect to $\Delta\Gamma$ up to the second order, we obtain

$$\frac{\langle F \rangle_{L+\Delta L} - \langle F \rangle_L}{\Delta L} = \left\langle \sum_{j=1}^N \frac{\langle \Delta\Gamma_j \rangle_{D,U}}{\Delta L} \frac{\partial F}{\partial \Gamma_j} + \frac{1}{2} \sum_{j,k=1}^N \frac{\langle \Delta\Gamma_j \Delta\Gamma_k \rangle_{D,U}}{\Delta L} \frac{\partial^2 F}{\partial \Gamma_j \partial \Gamma_k} \right\rangle_L, \tag{4.7}$$

where $\langle \cdots \rangle_D$ denoted the average over impurity configurations. Integrating by parts, we obtain a Fokker-Planck equation for $W(L; \Gamma)$ as

$$\frac{\partial W(L; \Gamma)}{\partial L} = \left[-\sum_{j=1}^N \frac{\partial}{\partial \Gamma_j} \frac{\langle \Delta\Gamma_j \rangle_{D,U}}{\Delta L} + \frac{1}{2} \sum_{j,k=1}^N \frac{\partial^2}{\partial \Gamma_j \partial \Gamma_k} \frac{\langle \Delta\Gamma_j \Delta\Gamma_k \rangle_{D,U}}{\Delta L} \right] W(L; \Gamma). \tag{4.8}$$

In order to obtain the small increment $\Delta\Gamma$ in Eq. (4.8), we add an infinitely small segment of length ΔL to the system with length L. The transfer matrix of the total system with length $L + \Delta L$ is also written by Eq. (4.2) where Γ, u, v, x, y are replaced with $\Gamma + \Delta\Gamma, u + \Delta u, v + \Delta v, x + \Delta x, y + \Delta y$, and satisfies the relation

$$T(\Gamma + \Delta\Gamma, u + \Delta u, v + \Delta v, x + \Delta x, y + \Delta y) = T'_{\Delta L} T(\Gamma, u, v, x, y), \tag{4.9}$$

where $T'_{\Delta L}$ is a transfer matrix for the small segment $L < x < L + \Delta L$ and given by

$$\begin{aligned} T'_{\Delta L} &= 1 + i \begin{bmatrix} -\gamma_{++} & \gamma_{+-} \\ -\gamma_{-+} & \gamma_{--} \end{bmatrix} - \frac{1}{2} \begin{bmatrix} -\gamma_{++} & \gamma_{+-} \\ -\gamma_{-+} & \gamma_{--} \end{bmatrix}^2, \\ (\gamma_{\pm\pm})_{\mu\nu} &= -\frac{1}{\hbar} \frac{1}{\sqrt{v_\mu v_\nu}} \langle \mu \pm | V(L, L + \Delta L) | \nu \pm \rangle, \end{aligned} \tag{4.10}$$

where $V(L, L + \Delta L)$ is the impurity potential in the segment $L < x < L + \Delta L$, and $|\nu\pm\rangle$ is the solution of the Schrödinger equation $H|\nu\pm\rangle = E_F|\nu\pm\rangle$ at the Fermi energy E_F with velocity $\pm v_\nu$. (ν is the index of the channel n for $\beta = 1$ and 2, or of the channel n and spin σ for $\beta = 4$.)

Expanding Eq. (4.9) in terms of $\Delta\Gamma, \Delta u, \Delta x(, \Delta v, \Delta y)$ up to the second order of γ (Born approximation), we obtain the first and second moments of the small increment

$\Delta\Gamma$. See Appendix A for details of derivation. The calculated result is as follows:

$$\langle \Delta\Gamma_j \rangle_D = \coth\Gamma_j \left\langle (R_{+-})_{jj}(R^\dagger_{+-})_{jj} \right\rangle_D + \sinh\Gamma_j \sum_{k\neq j} \frac{\left\langle (R_{+-})_{jk}(R^\dagger_{+-})_{kj} + (R^\dagger_{+-})_{jk}(R_{+-})_{kj} \right\rangle_D}{\cosh\Gamma_j - \cosh\Gamma_k}, \tag{4.11}$$

$$\langle \Delta\Gamma_j \Delta\Gamma_k \rangle_D = 2 \left\langle (R_{+-})_{jj}(R^\dagger_{+-})_{jj} \right\rangle_D \delta_{jk},$$

where $R_{+-} = u^\dagger \gamma_{+-} v$. In calculating Eq. (4.11), we have taken into account scattering processes like $\langle (\gamma_{++})_{nn'}(\gamma^\dagger_{++})_{n'n}\rangle_D$ or $\langle (\gamma_{+-})_{nn'}(\gamma^\dagger_{+-})_{n'n}\rangle_D$, which conserve the momentum in the x direction in a quantum wire after disorder averaging, although the forward-scattering terms vanish and the final result Eq. (4.11) depends only on back-scattering processes.

Using the assumption (B), we obtain the relation

$$\left\langle (R_{+-})_{jk}(R^\dagger_{+-})_{kj} + (R^\dagger_{+-})_{jk}(R_{+-})_{kj} \right\rangle_{D,U} = \frac{4\,(\beta/2)^{1-\delta_{jk}}}{(\beta(N-1)+2)l_H}, \tag{4.12}$$

where l_H is defined for $\beta = 1$ and 2 by

$$l_H^{-1} = \frac{1}{N} \sum_{n,n'=1}^{N} \left\langle |(\gamma_{+-})_{nn'}|^2 \right\rangle_D, \tag{4.13}$$

and for $\beta = 4$ by

$$l_H^{-1} = \frac{1}{N} \sum_{n,n'=1}^{N} \left\langle \left|(\gamma_{+-})_{n\uparrow n'\uparrow}\right|^2 + \left|(\gamma_{+-})_{n\uparrow n'\downarrow}\right|^2 \right\rangle_D. \tag{4.14}$$

When we assume an impurity potential of δ-function type and a hard-wall confinement potential in the lateral direction, l_H is given by

$$l_H^{-1} = \frac{1}{N} \frac{n_i \gamma^2}{\hbar^2} \sum_{n=1}^{N} \sum_{n'=1}^{N} \frac{1}{v_n v_{n'}} \int dy\ |\psi_{n+}(y)|^2\, |\psi_{n'-}(y)|^2, \tag{4.15}$$

where $\psi_{n\pm}(y)$ is the solution of Eq. (2.3) at $E = E_F$ with a velocity $\pm v_n$. For $\beta = 1$, l_H is given by the harmonic average

$$l_H^{-1} = \frac{1}{N} \sum_{n=1}^{N} l_n^{-1}, \tag{4.16}$$

where l_n is given in Eq. (3.12). (We will give a comment on this result in Sec. 4.3.) l_H is not in general the same as the mean free path of an electron in a two-dimensional system $l = v_F \tau = \hbar^3 v_F / m n_i \gamma^2$ (v_F : Fermi velocity). For example, Eq. (4.16) goes to

$1.27l$ in a large N limit when $B = 0$.

Substituting Eqs. (4.11) and (4.12) into Eq. (4.8), we finally obtain the desired Fokker-Planck equation for the distribution function W as

$$\frac{\partial W(s;\Lambda)}{\partial s} = \frac{2}{\beta(N-1)+2} \sum_{j=1}^{N} \frac{\partial}{\partial \Lambda_j}(1-\Lambda_j) \left[\frac{\partial}{\partial \Lambda_j}\Lambda_j^2 - \beta \sum_{k\neq j}^{N} \frac{\Lambda_j \Lambda_k}{\Lambda_j - \Lambda_k} \right] W(s;\Lambda), \tag{4.17}$$

with $\beta = 1, 2, 4$, where $s = L/l_H$, and $\Lambda_j = 2/(1+\cosh\Gamma_j)$ (we order Λ_j as $\Lambda_1 > \Lambda_2 > \cdots > \Lambda_N$). Exactly the same equation has been obtained in the case of a quasi-one-dimensional metallic wire for $\beta = 1$ and 2 by Mello *et al* [13, 15, 100] by use of the so-called maximum entropy method. However the mean free path has been introduced just as a parameter in this method.

4.2 Calculated Examples

It is difficult to obtain the general solution of $W(s;\Lambda)$ from Eq. (4.17), but several important transport quantities can be calculated. When the system is not in the strongly localized regime $L \ll \xi$ (ξ: localization length) and the channel number is sufficiently large, we can use a $1/N$ expansion method proposed by Mello *et al* [13, 15]. Details of calculation are shown in Appendix B. For $\beta = 1$ and 2, the calculated results are the same as those by Mello *et al.*, if we replace the mean free path used in Refs. 13 and 15 with l_H given by Eq. (4.13). The averaged dimensionless conductance per spin becomes

$$\langle g \rangle_s \equiv \frac{\langle G \rangle_s}{(e^2/h)} = \frac{N}{1+s} - \frac{1}{3}\frac{2-\beta}{\beta}\frac{s^3}{(1+s)^3} + O\left(\frac{1}{N}\right) \overset{L\gg l_H}{\longrightarrow} \frac{N l_H}{L} - \frac{\delta_{\beta 1}}{3} + \frac{\delta_{\beta 4}}{6}. \tag{4.18}$$

The first term corresponds to the Ohmic conductance and the second term to the correction according as the symmetry of the system. The variance of the conductance is given by

$$\mathrm{Var}(g) \equiv \langle g^2 \rangle_s - \langle g \rangle_s^2 = \frac{2}{\beta}\left(\frac{1}{15} - \frac{3}{5(1+s)^5} + \frac{1}{3(1+s)^6} \right) + O\left(\frac{1}{N}\right), \tag{4.19}$$

and the root-mean-squared fluctuation, including the factor 2 for spin degeneracy, is given by

$$\delta g = 2\sqrt{\mathrm{Var}(g)} \overset{L\gg l_H, N\gg 1}{\longrightarrow} \sqrt{\frac{8}{15\beta}} = \begin{cases} 0.730 & \text{for } \beta = 1 \\ 0.516 & \text{for } \beta = 2 \\ 0.365 & \text{for } \beta = 4 \end{cases}. \tag{4.20}$$

This result shows that, in the length region $l_H \ll L \ll \xi$ and in the large channel limit $N \gg 1$, the amplitude of the conductance fluctuation is universal also in a quantum wire and moreover the universal values are exactly the same as those in a metallic wire obtained by the perturbation treatment [8-11] for all β.

In the localized region, we have $\Lambda_1 \gg \Lambda_2 \gg \cdots \gg \Lambda_N$, and only one of Λ_i's is dominant in the conductance ($g \simeq \Lambda_1$). In this case the differential equation for the distribution function Eq. (4.8) is reduced to the one-channel problem

$$\frac{\partial W(\tilde{s};g)}{\partial \tilde{s}} = \left[\frac{\partial}{\partial g}(1-g)\frac{\partial}{\partial g}g^2\right] W(\tilde{s};g) \quad (\tilde{s} \equiv s/\xi), \tag{4.21}$$

where ξ is the localization length given by

$$\xi = \left(-\frac{\partial}{\partial L}\langle \ln g\rangle\right)^{-1}\Big|_{L\to\infty} = \begin{cases} (N+1)l_H/2 & (\beta=1) \\ Nl_H & (\beta=2) \\ (2N-1)l_H & (\beta=4) \end{cases} \overset{N\gg 1}{\longrightarrow} \beta N l_H/2. \tag{4.22}$$

Equation (4.21) has been solved exactly by Abrikosov [75], and the result is given by Eq. (2.28). Exact conductance, fluctuation, and distribution are also shown in Figs. 6 and 7. In a large channel-number limit the localization length ξ is proportional to the channel number and the symmetry factor, which is the same result given by several authors [86, 102, 108]. It is also noted that for a strictly one-dimensional wire ($N=1$), $\xi = l_H$ regardless of β. This is the result of the fact that the one-dimensional system always has the time-reversal and the spin-rotation symmetry.

4.3 Comparison with Numerical Results and Discussions

The above analytical results are compared in Figs. 30-33 with numerical results obtained in Chapter 2. In general the analytically calculated conductance is in good agreement with, but always a little smaller than the numerically calculated conductance. The analytically calculated localization length in Fig. 30 is considerably smaller than the numerical result. This deviation arises because the unitary matrices parametrizing the transfer matrix in Eq. (4.2) are not always distributed according to the invariant measure of $U(N)$ like the assumption (B). Under this assumption, the transmission probabilities T_n for the channel n is obtained as

$$T_n \equiv \langle (tt^\dagger)_{nn}\rangle_s = \sum_i \langle \Lambda_i\rangle_s \langle |u_{ni}|^2\rangle_U = \frac{1}{N}\sum_i \langle \Lambda_i\rangle_s = \frac{\langle g\rangle_s}{N}, \tag{4.23}$$

showing that each channel gives always the equal contribution to the conductance. Actually the numerical results in Chapter 2 seem to show that the distribution function of the unitary matrix deviates from the assumption (B) in such a way that the channel with a larger mean free path l_n tends to carry a larger current.

As seen in Eq. (4.17), the wire length is scaled by l_H. In the absence of magnetic field, l_H is equal to the harmonic average $l_H^{-1} = \sum l_n^{-1}/N$. This becomes quite unreasonable in the case that some channels have mean free paths much larger than others like in the presence of strong boundary-roughness scattering as mentioned in Chapter 2. In this case, both conductance and localization length are expected to be determined by

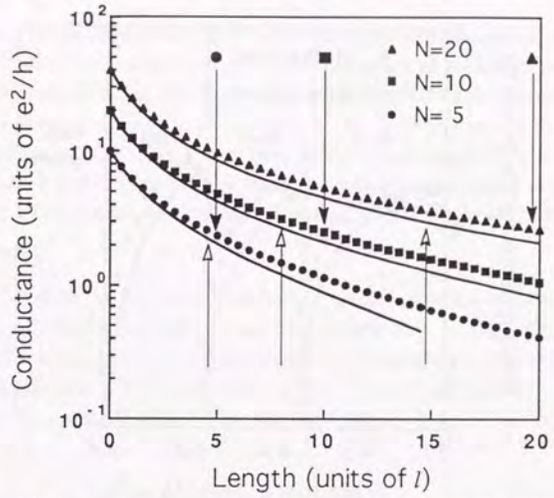

Fig. 30 Length dependence of conductance for various occupied channel numbers at $B = 0$, where l is the mean free path of an electron in a 2D system. Solid lines and upward arrows correspond to the analytically calculated conductance and localization length respectively, and symbols and downward arrows are the numerically calculated conductance and localization length respectively.

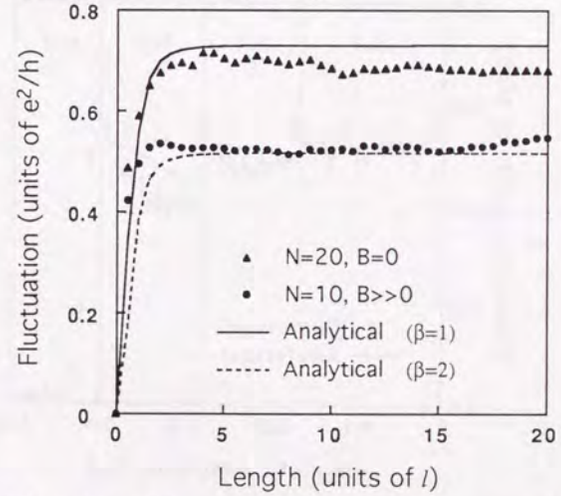

Fig. 31 Length dependence of fluctuation without and with a magnetic field. Solid line represents the analytical result with $\beta = 1$ and dotted line with $\beta = 2$. Symbols are the numerical results.

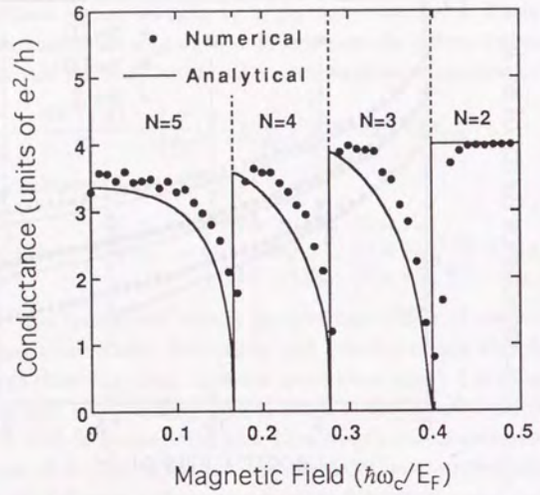

Fig. 32 Magnetic field dependence of conductance where $\omega_c = eB/m$. Solid line represents the analytical result with $\beta = 2$. The number of occupied subbands N changes at the magnetic fields indicated by the vertical dotted lines.

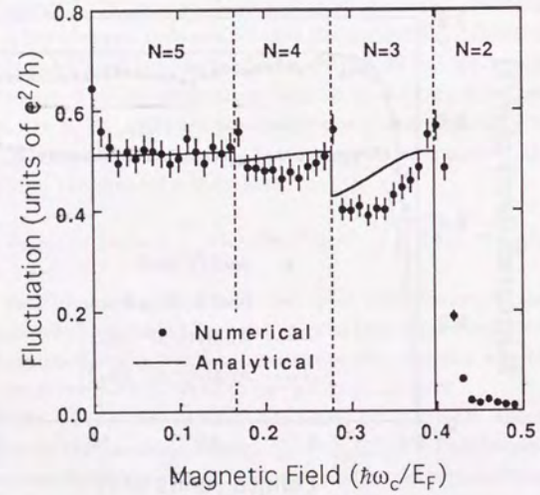

Fig. 33 Magnetic field dependence of fluctuation. Solid line represents the analytical result with $\beta = 2$.

channels with a larger mean free path. In the present result, however, they are determined by the harmonic average dominated by channels with a shorter mean free path. In Chapter 3, we showed that the mean free path appearing in conductance is given by the arithmetic average $l_A = \sum l_n/N$ ($\sim 1.6l$ in the large N limit and $B = 0$). This arithmetic average may be more appropriate as the length scale, since it does not seem to suffer from such difficulties. Further study, including going beyond our assumptions, is highly needed to understand this interesting and important problem.

4.4 Summary

We have studied the electrical transport in quantum wires analytically by use of the distribution function method. It has been shown that in the large channel limit the conductance fluctuation in a quantum wire is universal in the length region larger than the mean free path and shorter than the localization length and that the universal values are exactly the same as those in metallic wires.

Chapter 5
Persistent Currents in a Quantum Ring

In this chapter, we calculate persistent currents in a quantum ring by use of a diagrammatic perturbational method in order to examine the effect of well-defined subbands [43]. First we give a review of the previous works on persistent currents in metallic rings in Sec. 5.1. In Sec. 5.2 we describe the model. In Sec. 5.3 we calculate the typical currents. We also calculate in Sec. 5.4 the averaged current which is related to the root-squared-mean of fluctuation of the number of electrons. Finally we give conclusions in Sec. 5.5.

5.1 Persistent Currents in a Metallic Ring

Equilibrium persistent currents in normal metallic rings have attracted much attention since Büttiker, Imry and Landauer [28-30]. In the one-dimensional ring geometry, the presence of enclosed flux ϕ imposes a boundary condition on the wavefunction of an electron $\xi(x+L) = \exp(2\pi i\phi/\phi_0)\xi(x)$, where L is the circumference of the ring, $\xi(x) = L^{-1/2}\exp(ikx)$ for an ideal ring, and $\phi_0 = h/e$. With this boundary condition, the eigenvalue of the wavenumber k_n and the energy E_n are given by

$$\begin{aligned} k_n &= \frac{2\pi}{L}\left(n+\frac{\phi}{\phi_0}\right), \\ E_n &= \frac{\hbar^2}{2m}\left(\frac{2\pi}{L}\right)^2\left(n+\frac{\phi}{\phi_0}\right)^2, \ (n=0,\pm1,\pm2,\cdots). \end{aligned} \tag{5.1}$$

Then the persistent current in an ideal ring is calculated by

$$I = -\frac{\partial E}{\partial \phi} = -\sum_n \frac{\partial E_n}{\partial \phi}. \tag{5.2}$$

Substituting Eq. (5.1) into Eq. (5.2), we obtain

$$I = \begin{cases} -\frac{ev_F}{L}\frac{2\phi}{\phi_0} & \text{for odd } N_e \text{ and } -1/2 \le \frac{\phi}{\phi_0} \le 1/2, \\ -\frac{ev_F}{L}\left(\frac{2\phi}{\phi_0}-1\right) & \text{for even } N_e \text{ and } 0 \le \frac{\phi}{\phi_0} \le 1, \end{cases} \tag{5.3}$$

where N_e is the number of electrons. Eq. (5.3) can be expressed as a Fourier sum

$$I = \sum_{l=1}^{\infty} \frac{2I_0}{l\pi}\cos(lk_FL)\sin(2l\pi\phi/\phi_0), \tag{5.4}$$

where $N_e = k_FL/\pi$. Then the typical amplitude of persistent currents in a ring is estimated by $I \sim ev_F/L$ and the dominant periodicity is ϕ_0. This result is easy to understand if we note that $\tau = L/v_F$ is the time for an electron to make one turn around the ring and the value $I_0 = ev_F/L = e/\tau$ corresponds to the current carried by a single electron in the level near $E = E_F$. In the presence of weak scattering, we can obtain $I \sim I_0(l/L)$ if we replace τ with $\tau_D = L^2/D$ (D : diffusion constant) which corresponds to the time for an electron to move diffusively around the ring.

Experimental observation of the persistent currents was first made by Levy *et al.* [31] in the magnetization response of 10^7 isolated Cu rings with the ring circumference $L \sim 2.2\mu$m, the channel number in the transverse direction $N \sim 17000$, and the mean free path $l \sim 0.02\mu$m at a low temperature. They found that the average current has the value of order of $3\times10^{-3}ev_F/L$ per ring and the periodicity of $\phi_0/2$, not ϕ_0. This observation of the periodicity-halving was very surprising, although it was already predicted by Cheung *et al.* [33] and Bouchiat and Montambaux [34]. By the experimental evidence of $\phi_0/2$ periodicity, the importance of thermodynamic ensemble of the system to average has been clearly recognized. The experimental measurement was done under the condition of a *fixed number of electrons* in each ring (= the canonical ensemble), while the conventional diagrammatic method is applied for the system with *a fixed chemical potential* (= the grand-canonical ensemble). In an ideal 1D ring, we see from Eq. (5.4) that the lth Fourier coeffecient is proportional to $\cos(lk_FL) = \cos(l\pi N_e)$. If l is odd, this factor changes its sign as a function of N_e, while for even l it always gives unity. In the many-ring configuration, the number of electrons varies randomly from ring to ring, and only terms with even l survive. In the presence of weak disorder, it was shown [35-37] that the averaged current in the canonical ensemble is proportional to the root-mean-squared fluctuation of the number of electrons in the grand-canonical ensemble and that the averaged current had the $\phi_0/2$ periodicity and the magnitude was given at $T = 0$ by $\simeq (ev_F/L)(1/N)$. This magnitude of currents was smaller than the experiment by about order 2. Ambegaoker and Eckern [38] has taken into account the electron-electron interactions and also obtained the $\phi_0/2$ periodicity. But the magnitude of currents they obtained is still smaller than the experiment by about order one, although there is an ambiguity in selecting the electron-electron coupling constant which is experimentally unknown.

Recently another experiment was done by Chandrasekhar *et al.* [32] in a *single* ring of Au. The experiment was performed in two gold rings of diameters (a) 4μm and (b) 2.4μm and (c) a gold square loop of dimensions 1.4μm$\times2.6\mu$m with the channel

number $N \sim 50000$ and the mean free path $l \sim 0.07\mu$m. The magnetic response had a fundamental period of ϕ_0 and the amplitude of the oscillations corresponded to a persistent current at $T = 0$ of $(0.3 \sim 2.0)ev_F/L$. In the case of a single-ring system, the amplitude of the oscillation is calculated by the root-mean-squared fluctuation of currents $\delta I^2 = \langle I^2 \rangle - \langle I \rangle^2$ (which we call *typical current*) [39-41] It is shown that the difference of the ensemble is not so important for the typical current [34], and the typical current has been calculated by the grand-canonical ensemble in a normal metallic ring, given by $\delta I \simeq (ev_F/L)(l/L)$ with a ϕ_0 periodicity. Using parameters obtained in the experiment, the amplitude of currents at $T = 0$ is estimated as (a) 0.12nA, (b) 0.28nA, and (c) 0.25nA. The observed values in the experiment are (a) 3±2nA, (b) 30±15nA, and (c) 6±2nA, which are larger than the prediction by factor 25 to 100. Eckern and Schmid [42] have considered typical currents in the presence of electron-electron interactions and obtained $\delta I \simeq (ev_F/L)$ and the dominant periodicity of ϕ_0. But it is pointed out that, in addition to the ambiguity in determining the electron-electron coupling constant, they have taken into account only some of the relevant diagrams and their treatment is not appropriate [41].

5.2 Theoretical Model

We consider a two-dimensional ring of circumference L in the x direction, confined by potential in the y direction and threaded by a static magnetic flux ϕ inside the ring, as shown in Fig. 34. Without loss of generality, additional dimension (*i.e.*, z-direction) can be omitted for simplicity. We assume that the ring has a large aspect ratio, and neglect the influence of curvature of ring and the effect of a magnetic field threading in the plane of the ring.

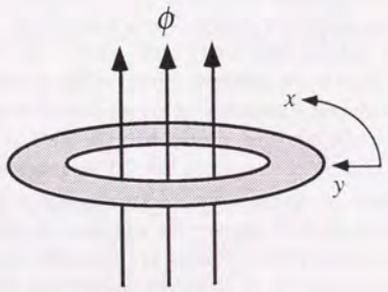

Fig. 34 Schematic ring with a circumference of L in the x direction. The ring is threaded by a magnetic flux ϕ.

We consider the same Hamiltonian Eq. (2.1), except that we adopt the gauge where the vector potential $\mathbf{A}$ points in the azimuthal (x) direction. The effect of a magnetic field can be eliminated by the gauge transformation. However, the wavefunction has a flux-periodic boundary condition in the x-direction as

$$\xi_{nk}(x + L, y) = \exp(2\pi i\phi/\phi_0)\xi_{nk}(x, y). \tag{5.1}$$

With this boundary condition, the wavenumber k is given by

$$k = \frac{2\pi}{L}(n_x + \phi/\phi_0), \quad (n_x = 0, \pm 1, \pm 2, \cdots). \tag{5.2}$$

By following the same arguments as in Sec. 3.1, we can show that, in quantum rings, the perturbated one-particle thermal Green function is diagonal with respect to the subband index and obtain in the Born approximation as

$$\langle G_n(k, i\varepsilon_m) \rangle = [i\hbar\varepsilon_m - \zeta_{nk} + i\Gamma_n \mathrm{sgn}\varepsilon_m]^{-1}, \tag{5.3}$$

where $\zeta_{nk} = \hbar^2k^2/2m - \hbar^2k_F^2/2m + E_n$ and $\hbar\varepsilon_m$ is the Matsubara frequencies for the fermion $\varepsilon_m = (2m+1)\pi/\beta = (2m+1)\pi k_B T$ and Γ_n is the imaginary part of self-energy of an electron in the channel n given by Eq. (3.9).

The ladder diagrams for finite temperatures in Fig. 35 can be obtained in the same way as shown in Sec. 3.3. We obtain the cooperon and the diffuson as

$$C_{nn'}(q, |\omega_j|) = D_{nn'}(q, |\omega_j|) = \frac{4\Gamma_n\Gamma_{n'}}{2\pi N(0)L}\left(Dq^2 + |\omega_j|\right)^{-1}, \quad \varepsilon_m(\varepsilon_m + \omega_j) < 0, \tag{5.4}$$

where $\omega_j = 2\pi j/\beta$, $N(0) = \sum_m (1/\pi\hbar v_m^F)$ is the total density of states (per spin) at the Fermi energy, and $D = (1/2\pi N(0))\sum_m v_m^F/\Gamma_m$ is the diffusion constant.

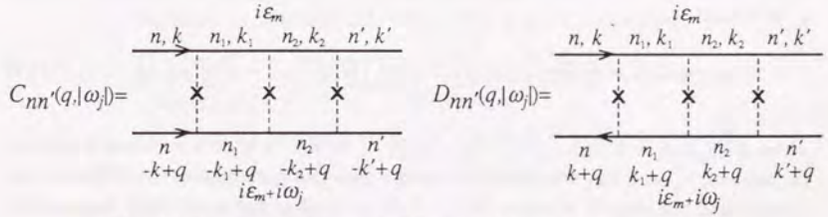

Fig. 35 Cooperon ladder and diffuson ladder at finite temperatures.

5.3 Typical Current

The thermodynamic equilibrium current is given in terms of the thermal Green function by

$$I = \frac{1}{\beta}\sum_{nk}\sum_{\varepsilon_m} G_n(k, i\varepsilon_m) I(k), \tag{5.5}$$

where $I(k) = -ev/L = -e\hbar k/mL$. Squaring and averaging over impurity configurations, we obtain the following expression.

$$\langle I^2\rangle = \frac{1}{\beta^2}\sum_{\varepsilon_m,\varepsilon_{m'}}\sum_{n,k,n',k'} I(k)I(k')\langle G_n(k, i\varepsilon_m)G_{n'}(k', i\varepsilon_{m'})\rangle. \tag{5.6}$$

The diagrams most contributing to the typical current $\delta I^2 = \langle I^2\rangle - \langle I\rangle^2$ are shown in Fig. 36, in which two current bubbles are connected by impurity lines.

The contribution from diagrams Fig. 36(a1) and (a2) is expressed by

$$\begin{aligned}(\delta I_a)^2 = \frac{1}{\beta^2}\sum_{\varepsilon_m(\varepsilon_m+\omega_j)<0}\sum_{n,k} I(k)^2\langle G_n(k, i\varepsilon_m)\rangle^2\langle G_n(k, i\varepsilon_m + i\omega_j)\rangle^2 \\ \times\sum_q \left(D_{nn}(q, |\omega_j|) - C_{nn}(q, |\omega_j|)\right),\end{aligned} \tag{5.7}$$

From the condition of the wavenumbers k, k' in Eq. (5.2), the momentum transfer $q = k \pm k'$ of a ladder should satisfy $q = k - k' = (2\pi/L)n_x$ for a diffuson and $q = k + k' = (2\pi/L)(n_x + 2\phi/\phi_0)$ for a cooperon ($n_x = 0, \pm1, \pm2, \cdots$). The vertex part is calculated as

$$\sum_k I(k)^2\langle G_n(k, i\varepsilon_m)\rangle^2\langle G_n(k, i\varepsilon_m + i\omega_j)\rangle^2 = \frac{e^2 v_n^F}{2L\hbar\Gamma_n^3}. \tag{5.8}$$

Substituting Eqs. (5.4) and (5.8) into Eq. (5.7) and summing over the subband index n, we obtain

$$(\delta I_a)^2 = \frac{1}{\beta^2}\frac{2e^2 D}{\hbar^2 L^2}\sum_{\varepsilon_m(\varepsilon_m+\omega_j)<0}\sum_q \left(\tilde{D}(q, |\omega_j|) - \tilde{C}(q, |\omega_j|)\right), \tag{5.9}$$

where $\tilde{D}(q, |\omega_j|) = \tilde{C}(q, |\omega_j|) = \left(Dq^2 + |\omega_j|\right)^{-1}$. In Eq. (5.9), the subband-dependent parameters, v_n^F and Γ_n, are collected together into two parameters, the diffusion constant D and the density of states $N(0)$. (It is noted that the same thing happened in Chapter 3.) Eq. (5.9) is exactly the same expression as that obtained for a metallic ring, if D and $N(0)$ are replaced with those for a metallic ring.

The q summation in Eq. (5.9) can be done in the same way in case of metallic rings and details of the calculation is shown in Appendix C. Changing the summation

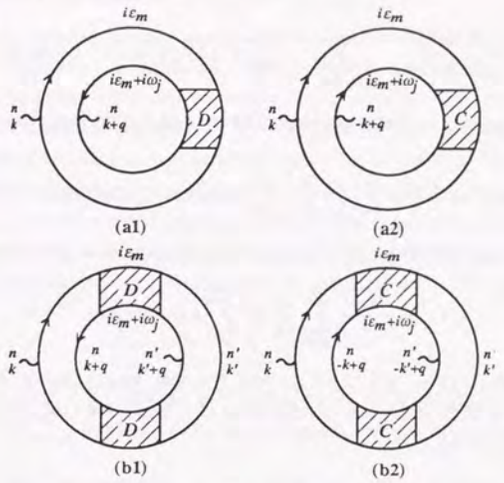

Fig. 36 Diagrams contributing to the typical current δI, where $(\delta I)^2 = \langle I^2\rangle - \langle I\rangle^2$. The current vertex is denoted by a wavy line, and a shaded part with D or C represents a diffuson or cooperon ladder respectively.

$\sum_{\varepsilon_m(\varepsilon_m+\omega_j)<0}$ to $\sum_{\omega_j>0}\hbar\omega_j/\pi k_B T$, we obtain

$$(\delta I_a)^2 = \frac{2k_B T}{\hbar}\sum_{j=1}^{\infty}\frac{\omega_j}{2\pi}\frac{2e^2}{\pi\alpha_j}\sum_{p=1}^{\infty}\sin^2 2\pi p\varphi\, e^{-2\pi\alpha_j p}, \tag{5.10}$$

where we defined $\alpha_j^2 \equiv |\omega_j|(L/2\pi)^2/D$ and $\varphi \equiv \phi/\phi_0$.

The contribution of diagrams (b1) and (b2) in Fig. 36 is expressed by

$$\begin{aligned}(\delta I_b)^2 = \frac{1}{\beta^2}\sum_{\varepsilon_m(\varepsilon_m+\omega_j)<0}\sum_{n,k,n',k'}\sum_q I(k)\langle G_n(k, i\varepsilon_m)\rangle^2\langle G_n(k+q, i\varepsilon_m + i\omega_j)\rangle \\ \times I(k'+q)\langle G_{n'}(k'+q, i\varepsilon_m)\rangle\langle G_{n'}(k', i\varepsilon_m + i\omega_j)\rangle^2 \\ \times\left(D_{nn'}^2(q, |\omega_j|) - C_{nn'}^2(q, |\omega_j|)\right).\end{aligned} \tag{5.11}$$

The vertex part is calculated as

$$\sum_k I(k)\langle G_n(k, i\varepsilon_m)\rangle^2\langle G_n(k+q, i\varepsilon_m + i\omega_j)\rangle = q\frac{ev_n^F}{2\Gamma_n^3}. \tag{5.12}$$

Substituting Eqs. (5.4) and (5.12) into Eq. (5.11) and summing over the subband index

n, n', we obtain

$$(\delta I_b)^2 = -\frac{1}{\beta^2}\frac{4e^2D^2}{\hbar^2L^2}\sum_{\varepsilon_m(\varepsilon_m+\omega_j)<0}\sum_q q^2\left(\tilde{D}^2(q,|\omega_j|)-\tilde{C}^2(q,|\omega_j|)\right). \tag{5.13}$$

The q summation can be done in the similar way as before (see Appendix C), and we obtain

$$(\delta I_b)^2 = \frac{2k_BT}{\hbar}\sum_{j=1}^{\infty}\frac{\omega_j}{2\pi}\frac{2e^2}{\pi\alpha_j}\sum_{p=1}^{\infty}(2\pi p\alpha_j-1)\sin^2 2\pi p\varphi e^{-2\pi\alpha_j p}. \tag{5.14}$$

By adding Eqs. (5.10) and (5.14), total typical current is given by

$$(\delta I)^2 = \frac{2k_BT}{\hbar}\sum_{j=1}^{\infty}\frac{\omega_j}{2\pi}4e^2\sum_{p=1}^{\infty}p\sin^2 2\pi p\varphi e^{-2\pi\alpha_j p}. \tag{5.15}$$

$\alpha_j^2 = |\omega_j|(L/2\pi)^2/D = j(L/L_T)^2$, where thermal length L_T is defined by $L_T = \sqrt{\hbar D/k_BT}$. At a sufficiently low temperature ($L_T \gg L$), we can change ω_j summation to integral over $x = \omega_j$,

$$\sum_{j=1}^{\infty}\frac{2k_BT}{\hbar}\frac{\omega_j}{2\pi}e^{-2\pi p\alpha_j} = \int_0^{\infty}dx\frac{1}{2\pi^2}xe^{-pL\sqrt{x/D}} = \frac{6}{\pi^2}\left(\frac{D}{L^2}\right)\frac{1}{p^4}, \tag{5.16}$$

and obtain

$$(\delta I)^2 = \frac{24}{\pi^2}\left(\frac{eD}{L^2}\right)^2\sum_{p=1}^{\infty}\frac{1}{p^3}\sin^2 2\pi p\phi/\phi_0. \tag{5.17}$$

When $L_T \ll L$, we can easily see from Eq. (5.15) that only $p = 1$ term in the p summation is dominant and the typical current is given by

$$(\delta I)^2 = \frac{2}{\pi^2}\left(\frac{eD}{L_T^2}\right)^2 e^{-2\pi L/L_T}\sin^2 2\pi\phi/\phi_0. \tag{5.18}$$

5.4 Averaged Current in a Single Ring

Next we calculate the average current $\langle I\rangle$ in a single ring. It has been pointed out [33, 35-37] that the there is a significant difference in the averaging results between the canonical and the grand-canonical ensemble. In a metallic ring, the average current for the canonical ensemble is given by $\langle I\rangle \sim (ev_F/L)(1/N)$, while the grand-canonical ensemble averaging causes the exponentially vanishing factor $\exp(-L/l)$.

In order to calculate the averaged current in a ring with a fixed number of electrons, we use the fact that the averaged current $I(N_e)$ in the canonical ensemble with a fixed number of electrons N_e is expressed in terms of the number fluctuation $\delta N_e(\mu)$ in the grand-canonical ensemble with a fixed chemical potential μ [35-37], such as

$$\langle I(N_e)\rangle = -\frac{\Delta}{2}\left\langle\frac{\partial}{\partial\phi}(\delta N_e(\mu))^2\right\rangle, \tag{5.19}$$

where $\Delta = \langle(\partial N_e/\partial\mu)_\phi\rangle$ is the mean level spacing and, for a quantum ring, it is given by $\Delta^{-1} = N(0)L = \sum_{n=1}^{N}(L/\pi\hbar v_n^F)$. The thermodynamic equilibrium number of electrons is given by

$$N_e = \frac{1}{\beta}\sum_{n,k}\sum_{\varepsilon_m}G_n(k,i\varepsilon_m). \tag{5.20}$$

Squaring Eq. (5.20) and averaging over disorder, we obtain the largest contribution as

$$\begin{aligned}\left\langle(\delta N_e)^2\right\rangle = \frac{1}{\beta^2}\sum_{\varepsilon_m(\varepsilon_m+\omega_j)<0}\sum_{n,k,n',k'}\sum_q &\langle G_n(k,i\varepsilon_m)\rangle^2\langle G_n(-k+q,i\varepsilon_m+i\omega_j)\rangle \\ &\times\langle G_{n'}(-k'+q,i\varepsilon_m)\rangle\langle G_{n'}(k',i\varepsilon_m+i\omega_j)\rangle^2 C_{nn'}^2(q,|\omega_j|),\end{aligned} \tag{5.21}$$

which is schematically shown in Fig. 37. It is noted that the diagram contains only cooperons because diffusons without the ϕ dependence do not contribute to the average current.

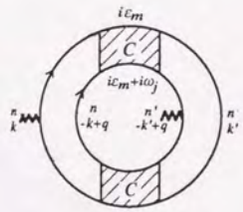

Fig. 37 Diagram contributing to the averaged current $I(N_e)$ for a fixed electron number N_e, where the vertex is the unit operator denoted by a zigzag line.

The calculation of Eq. (5.21) can be performed in the similar way as the typical current. The vertex part is evaluated as

$$\sum_k \langle G_n(k, i\varepsilon_m)\rangle^2 \langle G_n(-k+q, i\varepsilon_m + i\omega_j)\rangle = \frac{-iL}{2\hbar v_n^F \Gamma_n^2}. \tag{5.22}$$

Then Eq. (5.21) is reduced to

$$\left\langle (\delta N_e)^2 \right\rangle = \frac{1}{\beta^2} \sum_{\varepsilon_m(\varepsilon_m+\omega_j)<0} \sum_q \tilde{C}^2(q, |\omega_j|), \tag{5.23}$$

where subband-dependent parameters are collected again into the diffusion constant D. The q summation can be performed in the similar way as before (see Appendix C), and we obtain the averaged current as

$$\langle I(N_e)\rangle = \frac{e\Delta}{4\pi\hbar}\left(\frac{L}{L_T}\right)^2 \sum_{\omega_j>0} \frac{1}{\alpha_j} \sum_{p=1}^{\infty} p(1+2\pi p\alpha_j) \sin 4\pi p\varphi e^{-2\pi\alpha_j p}. \tag{5.24}$$

For $L_T \gg L$, the summation over ω_j results in

$$\langle I(N_e)\rangle = \frac{e\Delta}{2\pi^2\hbar} \sum_{p=1}^{\infty} \sin 4\pi p\phi/\phi_0, \tag{5.25}$$

and for $L_T \ll L$,

$$\langle I(N_e)\rangle = \frac{e\Delta}{2\hbar}\left(\frac{L}{L_T}\right)^2 \sin 4\pi\phi/\phi_0 e^{-2\pi L/L_T}. \tag{5.26}$$

5.5 Conclusion

We have seen that the typical current Eq. (5.15) and the averaged current Eq. (5.24) for a quantum ring become exactly the same expression as those for a metallic ring, if the diffusion constant D and the mean level spacing Δ for a quantum ring are replaced by those for a metallic ring. If we assume a hard-wall confinement potential and estimate the diffusion constant D and the mean level spacing Δ in a large channel limit $N \gg 1$, we find

$$\begin{aligned} &\Delta^{-1} = N(0)L = \sum_{n=1}^{N} L/\pi\hbar v_n^F \to NL/2\hbar v_F = (m/2\pi\hbar^2)LW, \\ &\sum_{n=1}^{N} (v_n^F/\Gamma_n)/2\pi N(0) \to v_F^2\tau/2, \end{aligned} \tag{5.27}$$

where v_F and τ are the Fermi velocity and the elastic-scattering time of electrons in a 2D system. Then Δ and D in a large channel limit are the same those for a 2D metallic ring.

From Eq. (5.17), the typical current δI at $T = 0$ has a magnitude of order $eD/L^2 \to (ev_F/L)(l/L)$ where l is the elastic mean free path in 2D system given by $l = v_F\tau$, and from Eq. (5.25), the averaged current at $T = 0$ is estimated as $e\Delta \to (ev_F/L)(1/N)$. Therefore, in a large channel limit, both the typical current and the averaged current are the same value as those for a 2D metallic ring. In conclusion, the well-defined subband structure in a quantum ring makes no effect on persistent currents.

Chapter 6

Summary

In this paper we have studied typical mesoscopic phenomena, like conductance fluctuations and persistent currents, in a quantum wire and ring by use of several methods of calculation, *i.e.*, numerical, perturbational, and distribution-function method.

In Chapter 2, we have numerically studied conductance fluctuations in quantum wires in the presence of magnetic fields, spin-orbit interaction, and boundary roughness. It has been shown that (i) when only a few subbands are occupied in the absence of magnetic field and spin-orbit interaction and in the presence of bulk impurities, there is no length region where the amplitude of fluctuations stays independent of L. When many subbands are occupied, ξ is much larger than l and there appears a universal region in $l \lesssim L \lesssim \xi$ where the universal value is close to that obtained for metallic wires by the perturbational method. We have also demonstrated that the crossover from quantum wires to metallic wires occurs when the broadening exceeds the subband energy separations. (ii) In the presence of a weak magnetic field or spin-orbit interaction, the amplitude of the conductance fluctuation is reduced in the universal region and the reduction-factor of the fluctuation is close to $1/\sqrt{2}$ and $1/2$ in the presence of magnetic fields and spin-orbit interaction respectively. (iii) Because of the peculiar nature of boundary-roughness scattering, the conductance fluctuation exhibits a different behavior from that for bulk impurities when the length is smaller than the localization length, *i.e.*, a singular enhancement of the fluctuation in the nearly ballistic region and the reduction of the fluctuation in the universal region from that of 1D metallic wires.

In Chapter 3 we have studied electrical transports in quantum wires by diagrammatic perturbational technique. We have calculated the conductance, the weak localization correction, and the conductance fluctuation. It has been shown that the amplitude of the universal conductance fluctuation is exactly the same as that in metallic wires.

In Chapter 4 we have studied the electrical transport in quantum wires analytically by use of the distribution function method. It has been shown that in the large channel limit the amplitude of the conductance fluctuation in a quantum wire is universal in the

length region larger than the mean free path and shorter than the localization length, and that the universal values are exactly the same as those in metallic wires for all the symmetries of the system.

In Chapter 5, persistent currents in a quantum ring have been calculated by a diagrammatic perturbational method. The typical current is obtained as $\delta I \sim (ev_F/L)(l/L)$ and the average current as $\langle I \rangle \sim (ev_F/L)(1/N)$. These expressions are the same as those for a metallic ring, and the well-defined subband structure makes no effect on the magnitude of persistent currents.

Appendix A

First we consider the case $\beta = 1$ and 2. Multiplying Eq. (4.9) by its Hermitian conjugate from the right, we obtain the equation

$$\begin{bmatrix} 1+u^\dagger\Delta u & 0 \\ 0 & 1+v^\dagger\Delta v \end{bmatrix} \begin{bmatrix} \cosh(\Gamma+\Delta\Gamma) & \sinh(\Gamma+\Delta\Gamma) \\ \sinh(\Gamma+\Delta\Gamma) & \cosh(\Gamma+\Delta\Gamma) \end{bmatrix} \begin{bmatrix} 1+\Delta u^\dagger u & 0 \\ 0 & 1+\Delta v^\dagger v \end{bmatrix}$$
$$= (1+iR-\frac{1}{2}R^2) \begin{bmatrix} \cosh\Gamma & \sinh\Gamma \\ \sinh\Gamma & \cosh\Gamma \end{bmatrix} (1-iR^\dagger-\frac{1}{2}R^{\dagger 2}), \tag{A.1}$$

where the matrix R is defined by

$$R = \begin{bmatrix} -u^\dagger\gamma_{++}u & u^\dagger\gamma_{+-}v \\ -v^\dagger\gamma_{-+}u & v^\dagger\gamma_{--}v \end{bmatrix} \equiv \begin{bmatrix} R_{++} & R_{+-} \\ R_{-+} & R_{--} \end{bmatrix}. \tag{A.2}$$

In order to calculate $\Delta\Gamma, \Delta u, \Delta v, \Delta x, \Delta y$ up to the second order of γ (Born approximation), we separate the small increment $\Delta P(= \Delta\Gamma, \Delta u, \Delta v, \Delta x, \Delta y)$ into two parts, $\Delta P = \Delta_1 P + \Delta_2 P$, where $\Delta_1 P$ contains terms of the first order of γ and $\Delta_2 P$ contains terms of the second order of γ. First we will calculate $\Delta_1 P$. Expanding Eq. (A.1) in terms of $\Delta\Gamma, \Delta u, \Delta v, \Delta x$ and Δy up to the first order of γ, we obtain the equation of the sub-matrix in the upper-left block of Eq. (A.1) as

$$\sinh\Gamma\Delta_1\Gamma + [u^\dagger\Delta_1 u]\cosh\Gamma + \cosh\Gamma\,[\Delta_1 u^\dagger u] = i(R_{++}\cosh\Gamma + R_{+-}\sinh\Gamma) - i(\cosh\Gamma R_{++}^\dagger + \sinh\Gamma R_{+-}^\dagger). \tag{A.3}$$

The diagonal part of Eq. (A.3) is calculated as

$$\sinh\Gamma_j\Delta_1\Gamma_j + \cosh\Gamma_j\left([u^\dagger\Delta_1 u]_{jj} + [\Delta_1 u^\dagger u]_{jj}\right) = i\sinh\Gamma_j\left\{(R_{+-})_{jj} - (R_{+-}^\dagger)_{jj}\right\}, \tag{A.4}$$

where we used the relation $R_{+-} = -R_{-+}^\dagger$, $R_{++} = R_{++}^\dagger$. As the matrix u must satisfy the unitarity $(u^\dagger + \Delta u^\dagger)(u + \Delta u) = 1$, we obtain the relation

$$u^\dagger\Delta u + \Delta u^\dagger u = -[u^\dagger\Delta u]\,[\Delta u^\dagger u]. \tag{A.5}$$

From Eq. (A.5), we can see that $u^\dagger\Delta_1 u + \Delta_1 u^\dagger u$ is the second-order contribution, and we obtain $\Delta_1\Gamma$ as

$$\Delta_1\Gamma_j = i\left\{(R_{+-})_{jj} - (R_{+-}^\dagger)_{jj}\right\}. \tag{A.6}$$

The off-diagonal part of Eq. (A.3) is given by

$$[u^\dagger\Delta_1 u]_{jk} = i(R_{++})_{jk} - i\frac{(R_{+-})_{jk}\sinh\Gamma_k - \sinh\Gamma_j(R_{+-}^\dagger)_{jk}}{\cosh\Gamma_j - \cosh\Gamma_k}, \tag{A.7}$$

where we used the relation $u^\dagger\Delta_1 u = -\Delta_1 u^\dagger u$ up to order γ.

Next we consider the second order of γ. The left-hand-side of the left-upper block of Eq. (A.1) of order γ^2 is given by

$$\sinh\Gamma\Delta_2\Gamma + \frac{1}{2}\cosh\Gamma\,(\Delta_1\Gamma)^2 + [u^\dagger\Delta u]\cosh\Gamma + \cosh\Gamma\,[\Delta u^\dagger u] + [u^\dagger\Delta_1 u]\cosh\Gamma\,[\Delta_1 u^\dagger u] + [u^\dagger\Delta_1 u]\sinh\Gamma\Delta_1\Gamma + \sinh\Gamma\Delta_1\Gamma\,[\Delta_1 u^\dagger u]. \tag{A.8}$$

Using Eq. (A.5), the second line of Eq. (A.8) is calculated as

$$[u^\dagger\Delta u]_{jj}\cosh\Gamma_j + \cosh\Gamma_j\,[\Delta u^\dagger u]_{jj} + [u^\dagger\Delta_1 u\cosh\Gamma\Delta_1 u^\dagger u]_{jj} = \sum_k(\cosh\Gamma_k - \cosh\Gamma_j)\,[u^\dagger\Delta_1 u]_{jk}\,[\Delta_1 u^\dagger u]_{kj} + O(\gamma^3), \tag{A.9}$$

and the third line by $[u^\dagger\Delta_1 u]_{jj}\sinh\Gamma_j\Delta_1\Gamma_j + \sinh\Gamma_j\Delta_1\Gamma_j\,[\Delta_1 u^\dagger u]_{jj} = O(\gamma^3)$. Then the diagonal part of Eq. (A.8) is obtained as

$$\sinh\Gamma_j\Delta_2\Gamma_j + \frac{1}{2}\cosh\Gamma_j\,(\Delta_1\Gamma_j)^2 + \sum_k(\cosh\Gamma_k - \cosh\Gamma_j)\,[u^\dagger\Delta_1 u]_{jk}\,[\Delta_1 u^\dagger u]_{kj}. \tag{A.10}$$

In calculating the right-hand side of Eq. (A.1), we only have to take into accounts scattering processes like $\langle(\gamma_{++})_{nn'}(\gamma_{++}^\dagger)_{n'n}\rangle_D$ or $\langle(\gamma_{+-})_{nn'}(\gamma_{+-}^\dagger)_{n'n}\rangle_D$, which conserve the momentum in the x direction in a quantum wire after disorder averaging. Ignoring non-contributing terms, we obtain the right-hand side of the left-upper block of Eq. (A.1) of order of γ^2 as

$$\sum_k(\cosh\Gamma_k - \cosh\Gamma_j)\,(R_{++})_{jk}(R_{++}^\dagger)_{kj} + \sum_k(\cosh\Gamma_k + \cosh\Gamma_j)\,(R_{+-})_{jk}(R_{+-}^\dagger)_{kj}. \tag{A.11}$$

Then the first moment $\langle\Delta\Gamma\rangle_D = \langle\Delta_2\Gamma\rangle_D$ is calculated from Eqs. (A.10) and (A.11) as

$$\langle\Delta\Gamma_j\rangle_D = \coth\Gamma_j\left\langle(R_{+-})_{jj}\,(R_{+-}^\dagger)_{jj}\right\rangle_D + \sinh\Gamma_j\sum_{k\neq j}\frac{\left\langle(R_{+-})_{jk}(R_{+-}^\dagger)_{kj} + (R_{+-}^\dagger)_{jk}(R_{+-})_{kj}\right\rangle_D}{\cosh\Gamma_j - \cosh\Gamma_k}, \tag{A.12}$$

and, squaring Eq. (A.6), the second moment $\langle\Delta\Gamma_j\Delta\Gamma_k\rangle_D = \langle\Delta_1\Gamma_j\Delta_1\Gamma_k\rangle_D$ as

$$\langle\Delta\Gamma_j\Delta\Gamma_k\rangle_D = 2\langle(R_{+-})_{jj}(R_{+-}^\dagger)_{jj}\rangle_D\delta_{jk}. \tag{A.13}$$

Adding Eqs. (A.12) and (A.13), we obtain Eq. (4.11)

In the presence of strong spin-orbit scatterings ($\beta = 4$), the symmetry of the system is symplectic. In this case, a convenient way of calculation is to express numbers in terms

of quaternions. A quaternion is itself 2×2 matrix, given by

$$q = q_0 + q_1\tau_1 + q_2\tau_2 + q_3\tau_3 \equiv q_0 + (q \cdot \tau), \tag{A.14}$$

where, for (μ, ν, λ) as an even permutation of $(1, 2, 3)$,

$$\tau_1 = \begin{bmatrix} i & 0 \\ 0 & -i \end{bmatrix}, \ \tau_2 = \begin{bmatrix} 0 & -1 \\ 1 & 0 \end{bmatrix}, \ \tau_3 = \begin{bmatrix} 0 & -i \\ -i & 0 \end{bmatrix}, \tag{A.15}$$
$$(\tau_\mu)^2 = -1, \ \tau_\mu\tau_\nu = -\tau_\nu\tau_\mu = \tau_\lambda.$$

Any $2N \times 2N$ matrix with complex elements can be cut into N^2 blocks of 2×2 matrices and considered as an $N \times N$ matrix with complex quaternion elements.

For a quaternion q given by Eq. (A.14), we define a "conjugate quaternion" by $\bar{q} = q_0 - (q \cdot \tau)$, its "complex conjugate" by $q^c = q_0^* + (q^* \cdot \tau)$, and the "Hermitian conjugate" by $q^\dagger = q_0^* + (q^* \cdot \tau)$. q is called "quaternion scalar" when it satisfies the relation $\bar{q} = q$ and then is a diagonal matrix with the same matrix element q_0. For an $N \times N$ matrix Q with quaternion elements $q_{\mu\nu}$, its transposition is given by $(Q^T)_{\mu\nu} = \tau_2\overline{q_{\nu\mu}}\tau_2^T$, its Hermitian conjugation by $(Q^\dagger)_{\mu\nu} = q^\dagger_{\nu\mu}$, and its time-reversal by $(Q^R)_{\mu\nu} = \overline{q_{\nu\mu}}$. In the following, we denote quaternions with greek subscripts and scalar numbers with roman subscripts.

The transfer matrix for a system with the symplectic symmetry satisfies the condition of time-reversality for the system with spin 1/2

$$T^* = KTK^T, \ K = \begin{bmatrix} 0 & \kappa \\ \kappa & 0 \end{bmatrix}, \tag{A.16}$$

where κ is defined in Eq. (4.3). The transfer matrix for an infinitely small segment is given by Eq. (4.10), except that the matrix elements of $\gamma_{\pm\pm}$ are quaternions. Noting that Eq. (4.10) satisfies Eq. (A.16), we can derive the relation $(\gamma_{+-})^* = \kappa\gamma_{-+}\kappa^T$. Moreover the matrix elements of the scattering potential must be Hermitian, *i.e.*, $\gamma^\dagger_{+-} = \gamma_{-+}$. From these two relations, γ_{+-} satisfies the condition

$$\gamma_{+-} = \kappa\gamma_{+-}^T\kappa^T = \gamma^R_{+-}. \tag{A.17}$$

Except that elements of the transfer matrix are quaternions, the derivation of the small increments of parameter $\Delta\Gamma$ is almost the same as for $\beta = 1$ and 2. Adding the small segment $T'_{\Delta L}$ to the system with length L and expanding Eq. (4.9) in terms of small parameters, we obtain the same expression as Eq. (4.11), if we replace j and k to μ and ν respectively and treat $(R_{+-})_{\mu\nu} = (u^\dagger\gamma_{+-}u^c)_{\mu\nu}$ as quaternions. (Γ_μ are quaternion scalar with diagonal elements Γ_j of real numbers, and we can treat them just as real numbers.) Noting the relation Eq. (A.17), we can show that

$$\overline{(R_{+-})_{\mu\nu}} = \sum_{\mu',\nu'} \overline{(u_{\mu'\mu})^\dagger(\gamma_{+-})_{\mu'\nu'}u^c_{\nu'\nu}} = \sum_{\mu',\nu'} (u_{\nu'\nu})^\dagger\overline{(\gamma_{+-})_{\mu'\nu'}}u^c_{\mu'\mu} = (R_{+-})_{\nu\mu},$$
$$\overline{(R_{+-})_{\mu\nu}(R^\dagger_{+-})_{\nu\mu}} = (R_{+-})^c_{\mu\nu}\overline{(R_{+-})_{\mu\nu}} = (R^\dagger_{+-})_{\mu\nu}(R_{+-})_{\nu\mu}. \tag{A.18}$$

Therefore $\langle\Delta\Gamma_\mu\rangle_D$ and $\langle(\Delta\Gamma_\mu)^2\rangle_D$ are quaternion scalar. By averaging over the unitary matrix u, we obtain the results

$$\left\langle (R_{+-})_{\mu\mu}(R^\dagger_{+-})_{\mu\mu} \right\rangle_{D,U} = \frac{1}{(2N-1)l_H} \times 1_2,$$
$$\left\langle (R_{+-})_{\mu\nu}(R^\dagger_{+-})_{\nu\mu} + (R^\dagger_{+-})_{\mu\nu}(R_{+-})_{\nu\mu} \right\rangle_{D,U} = \frac{4}{(2N-1)l_H} \times 1_2, \tag{A.19}$$
$$l_H^{-1} = \frac{1}{N}\sum_{n,n'=1}^{N} \left\langle \left|(\gamma_{+-})_{n\uparrow n'\uparrow}\right|^2 + \left|(\gamma_{+-})_{n\uparrow n'\downarrow}\right|^2 \right\rangle_D,$$

where 1_2 is a 2×2 unit matrix.

Appendix B

By use of Eq. (4.8), the expectation value of p-th moment $\langle g^p \rangle_s$ of dimensionless conductance $g = G/(e^2/h)$ satisfies the following ordinary equation:

$$\frac{\beta N + 2 - \beta}{2} \partial_s \langle g^p \rangle_s = \left\langle -\beta p g^{p+1} - (2-\beta) p g^{p-1} g_2 + 2p(p-1) g^{p-2}(g_2 - g_3) \right\rangle_s , \quad \text{(B.1)}$$

where $\partial_s = d/ds$. The right-hand-side of Eq. (B.1) contains three kinds of moment other than $\langle g^p \rangle_s$, then we write down equations for these moments:

$$\begin{aligned}
\frac{\beta N + 2 - \beta}{2} \partial_s \langle g^{p-1} g_2 \rangle_s &= \langle 2\beta g^{p+1} - \beta(p+3) g^p g_2 + 2(2-\beta) g^{p-1} g_2 \\
&\quad -4(2-\beta) g^{p-1} g_3 - (2-\beta)(p-1) g^{p-2} g_2^2 \rangle_s \\
&\quad + \langle 8(p-1) g^{p-2}(g_3 - g_4) + 2(p-1)(p-2) g^{p-3}(g_2^2 - g_2 g_3) \rangle_s , \\
\frac{\beta N + 2 - \beta}{2} \partial_s \langle g^{p-1} g_3 \rangle_s &= \langle -\beta(p+5) g^p g_3 + 6\beta g^p g_2 - 3\beta g^{p-1} g_2^2 \rangle_s \\
&\quad + \langle 2(p-1)(p-2) g^{p-3} g_3 (g_2 - g_3) + 12(p-1) g^{p-2}(g_5 - g_4) \\
&\quad - 2(2-\beta)(p-1) g^{p-2} g_2 g_3 - 18(2-\beta) g^{p-1} g_4 \\
&\quad + 12(2-\beta) g^{p-1} g_3 \rangle_s , \\
\frac{\beta N + 2 - \beta}{2} \partial_s \langle g^{p-2} g_2^2 \rangle_s &= \langle -\beta(p+6) g^{p-1} g_2^2 + 4\beta g^p g_2 \rangle_s \\
&\quad + \langle 2(p-2)(p-3) g^{p-4} g_2^2 (g_2 - g_3) - 16(p-2) g^{p-3} g_2 (g_4 - g_3) \\
&\quad - 16 g^{p-2}(g_5 - g_4) - (2-\beta)(p-2) g^{p-3} g_2^3 \\
&\quad - 4(2-\beta) g^{p-2} g_2 (2 g_3 - g_2) \rangle_s .
\end{aligned} \quad \text{(B.2)}$$

We can see that new kinds of moment appear in Eq. (B.2), and it seems impossible to continue to write down and find the general solution of these coupled equations. Instead we seek an approximate solution. When the channel number N is sufficiently large and the system is not in the localized regime ($L \ll N l_H$), we can expand transport quantities in terms of N. In this regime, we are concerned with the moments of conductance up to second order and we need to obtain the first three expansion terms. For this purpose, we only have to calculate four quantities, $\langle T^p \rangle_s$, $\langle T^{p-1} T_2 \rangle_s$, $\langle T^{p-1} T_3 \rangle_s$, and $\langle T^{p-2} T_2^2 \rangle_s$. In the right-hand-sides of Eq. (B.2), these quantities are collected in the first angular brackets. Expansion of four quantities is as follows:

$$\begin{aligned}
\langle g^p \rangle_s &= N^p a_{p,0} + N^{p-1} a_{p,1} + N^{p-2} a_{p,2} + \cdots , \\
\langle g^{p-1} g_2 \rangle_s &= N^p b_{p,0} + N^{p-1} b_{p,1} + N^{p-2} b_{p,2} + \cdots , \\
\langle g^{p-1} g_3 \rangle_s &= N^p c_{p,0} + N^{p-1} c_{p,1} + N^{p-2} c_{p,2} + \cdots , \\
\langle g^{p-2} g_2^2 \rangle_s &= N^p d_{p,0} + N^{p-1} d_{p,1} + N^{p-2} d_{p,2} + \cdots ,
\end{aligned} \quad \text{(B.3)}$$

where the initial conditions are

$$a_{p,m}(0) = b_{p,m}(0) = c_{p,m}(0) = d_{p,m}(0) = \delta_{m0}. \quad \text{(B.4)}$$

Substituting Eq. (B.3) into Eqs. (B.1) and (B.2), we obtain the coupled equations for a, b, c and d

$$\begin{aligned}
&(\beta N + 2 - \beta)\left(N^p \partial_s a_{p,0}(s) + N^{p-1} \partial_s a_{p,1}(s) + N^{p-2} \partial_s a_{p,2}(s)\right) \\
&\quad = -\beta p \left(N^{p+1} a_{p+1,0}(s) + N^p a_{p+1,1}(s) + N^{p-1} a_{p+1,2}(s) + \cdots\right) \\
&\qquad - (2-\beta) p \left(N^p b_{p,0}(s) + N^{p-1} b_{p,1}(s) + \cdots\right) \\
&\qquad + 2p(p-1)\left(N^{p-1} b_{p-1,0}(s) + \cdots\right) - 2p(p-1)\left(N^{p-1} c_{p-1,0}(s) + \cdots\right), \\
&(\beta N + 2 - \beta)\left(N^p \partial_s b_{p,0}(s) + N^{p-1} \partial_s b_{p,1}(s) + \cdots\right) \\
&\quad = 2\beta \left(N^{p+1} a_{p+1,0}(s) + N^p a_{p+1,1}(s) + \cdots\right) \\
&\qquad - \beta(p+3)\left(N^{p+1} b_{p+1,0}(s) + N^p b_{p+1,1}(s) + \cdots\right) \\
&\qquad + 2(2-\beta)\left(N^p b_{p,0}(s) + \cdots\right) - 4(2-\beta)\left(N^p c_{p,0}(s) + \cdots\right) \\
&\qquad - (2-\beta)(p-1)\left(N^p d_{p,0}(s) + \cdots\right) + O(N^{p-1}), \\
&(\beta N + 2 - \beta)\left(N^p \partial_s c_{p,0}(s) + \cdots\right) \\
&\quad = -\beta(p+5)\left(N^{p+1} c_{p+1,0}(s) + \cdots\right) + 6\beta\left(N^{p+1} b_{p+1,0}(s) + \cdots\right) \\
&\qquad - 3\beta\left(N^{p+1} d_{p+1,0}(s) + \cdots\right) + O(N^p), \\
&(\beta N + 2 - \beta)\left(N^p d_{p,0}(s) + \cdots\right) \\
&\quad = -\beta(p+6)\left(N^{p+1} d_{p+1,0}(s) + \cdots\right) + 4\beta\left(N^{p+1} b_{p+1,0}(s) + \cdots\right) + O(N^p).
\end{aligned} \quad \text{(B.5)}$$

Equating the coefficients of N^{p+1}, N^p, and N^{p-1} in Eq. (B.5), we obtain the differential equations

$$\partial_s a_{p,0}(s) + p a_{p+1,0}(s) = 0, \quad \text{(B.6a)}$$

$$(2-\beta)\partial_s a_{p,0}(s) + \beta \partial_s a_{p,1}(s) = -(2-\beta) p b_{p,0}(s) - \beta p a_{p+1,1}(s), \quad \text{(B.6b)}$$

$$\begin{aligned}
(2-\beta)\partial_s a_{p,1}(s) + \beta \partial_s a_{p,2}(s) = &-\beta p a_{p+1,2}(s) - (2-\beta) p b_{p,1}(s) \\
&+ 2p(p-1) b_{p-1,0}(s) - 2p(p-1) c_{p-1,0}(s),
\end{aligned} \quad \text{(B.6c)}$$

$$\partial_s b_{p,0}(s) = 2a_{p+1,0}(s) - (p+3) b_{p+1,0}(s), \quad \text{(B.6d)}$$

$$\begin{aligned}
(2-\beta)\partial_s b_{p,0}(s) + \beta \partial_s b_{p,1}(s) = &2\beta a_{p+1,1}(s) - \beta(p+3) b_{p+1,1}(s) \\
&+ 2(2-\beta) b_{p,0}(s) - 4(2-\beta) c_{p,0}(s) - (2-\beta)(p-1) d_{p,0}(s),
\end{aligned} \quad \text{(B.6e)}$$

$$\partial_s c_{p,0}(s) = -(p+5) c_{p+1,0}(s) + 6 b_{p+1,0}(s) - 3 d_{p+1,0}(s), \quad \text{(B.6f)}$$

$$\partial_s d_{p,0}(s) = -(p+6) d_{p+1,0}(s) + 4 b_{p+1,0}(s). \quad \text{(B.6g)}$$

From Eq. (B.6a) and the condition $a_{p,0}(0) = 1$, we obtain

$$\partial_s^{(n)} a_{p,0}(0) = (-p)(-p-1)\cdots(p-n+1), \tag{B.7}$$

and therefore the solution for $a_{p,0}(s)$ is

$$a_{p,0}(s) = (1+s)^{-p}. \tag{B.8}$$

Inserting Eq. (B.8) into Eq. (B.6d) and solving the equation, we obtain

$$b_{p,0}(s) = \frac{2}{3}\frac{1}{(1+s)^p} + \frac{1}{3}\frac{1}{(1+s)^{p+3}}. \tag{B.9}$$

Then substituting Eqs. (B.8) and (B.9) into Eq. (B.6b) and (B.6g), we find

$$\begin{aligned} a_{p,1}(s) &= \frac{2-\beta}{\beta}\left[-\frac{p}{3}\frac{1}{(1+s)^{p-1}} + \frac{p}{(1+s)^p} - \frac{p}{(1+s)^{p+1}} + \frac{p}{3}\frac{1}{(1+s)^{p+2}}\right] \\ &= -\frac{2-\beta}{3\beta}\frac{ps^3}{(1+s)^{p+2}}, \end{aligned} \tag{B.10}$$

and

$$d_{p,0}(s) = \frac{4}{9}\frac{1}{(1+s)^p} + \frac{4}{9}\frac{1}{(1+s)^{p+3}} + \frac{1}{9}\frac{1}{(1+s)^{p+6}}. \tag{B.11}$$

Repeating the same procedures, we can solve the coupled equations (B.6a)-(B.6g), and the results are

$$\begin{aligned} c_{p,0}(s) =& \frac{8}{15}\frac{1}{(1+s)^p} + \frac{1}{3}\frac{1}{(1+s)^{p+3}} - \frac{3}{15}\frac{1}{(1+s)^{p+5}} + \frac{1}{3}\frac{1}{(1+s)^{p+6}}, \\ b_{p,1}(s) =& \frac{2-\beta}{\beta}\left[-\frac{10p+4}{45}\frac{1}{(1+s)^{p-1}} + \frac{2p}{3}\frac{1}{(1+s)^p} - \frac{2p}{3}\frac{1}{(1+s)^{p+1}} + \frac{p+1}{9}\frac{1}{(1+s)^{p+2}}\right. \\ &\left. + \frac{p+3}{3}\frac{1}{(1+s)^{p+3}} - \frac{5p+27}{15}\frac{1}{(1+s)^{p+4}} + \frac{p+7}{9}\frac{1}{(1+s)^{p+5}}\right], \\ a_{p,2}(s) =& \left(\frac{2-\beta}{\beta}\right)^2 p\left[\frac{11p-9}{90}\frac{1}{(1+s)^{p-2}} + \frac{-p+1}{3}\frac{1}{(1+s)^{p-1}} + \frac{5p-5}{6}\frac{1}{(1+s)^p}\right. \\ &+ \frac{-10p+3}{9}\frac{1}{(1+s)^{p+1}} + \frac{5p+7}{6}\frac{1}{(1+s)^{p+2}} \\ &\left. + \frac{-11p-16}{15}\frac{1}{(1+s)^{p+3}} + \frac{7p+3}{18}\frac{1}{(1+s)^{p+4}}\right] \\ &+ \frac{2(\beta-1)(4-\beta)}{\beta^2} p\left[\frac{3p-5}{90}\frac{1}{(1+s)^{p-2}} + \frac{1}{9}\frac{1}{(1+s)^{p+1}}\right. \\ &\left. + \frac{-p}{5}\frac{1}{(1+s)^{p+3}} + \frac{3p-1}{18}\frac{1}{(1+s)^{p+4}}\right]. \end{aligned} \tag{B.12}$$

Substituting Eqs. (B.8), (B.10) and (B.12) into Eq. (B.3), the p-th moment of conductance is given by

$$\begin{aligned} \langle g^p \rangle &= N^p a_{p,0}(s) + N^{p-1} a_{p,1}(s) + N^{p-2} a_{p,2}(s) + \cdots \\ &= \frac{N^p}{(1+s)^p} - N^{p-1}\frac{2-\beta}{3\beta}\frac{ps^3}{(1+s)^{p+2}} + \cdots, \end{aligned} \tag{B.13}$$

and the variance of conductance is calculated as

$$\begin{aligned} \mathrm{Var}(g) =& \langle g^2 \rangle - \langle g \rangle^2 \\ =& \left(N^2 a_{2,0}(s) + N a_{2,1}(s) + a_{2,2}(s)\right) - \left(N a_{1,0}(s) + a_{1,1}(s) + N^{-1} a_{1,2}(s)\right)^2 \\ =& N^2\left(a_{2,0}(s) - a_{1,0}(s)^2\right) + N\left(a_{2,1}(s) - 2a_{1,0}(s)a_{1,1}(s)\right) \\ &+ \left(a_{2,2}(s) - a_{1,1}(s)^2 - 2a_{1,0}(s)a_{1,2}(s)\right) + \cdots \\ =& \frac{2}{\beta}\left(\frac{1}{15} - \frac{3}{5(1+s)^5} + \frac{1}{3(1+s)^6}\right) + O\left(\frac{1}{N}\right) \end{aligned} \tag{B.14}$$

Finally, it is noted that the expansion coefficients in Eq. (B.3), such as $a_{p,n}$, are dependent on the sample length L, and $1/N$ expansion used here becomes invalid when the sample length becomes larger than the localization length Nl_H, because expanded terms become comparable in order and $1/N$ is no longer suitable for an expansion parameter.

Appendix C

The q summation of Eq. (5.9) is performed as follows.

$$\begin{aligned}
&\sum_q \left(\tilde{D}\left(q,|\omega_j|\right)-\tilde{C}\left(q,|\omega_j|\right)\right) \\
&=\sum_{n_x=-\infty}^{\infty}\left(\frac{1}{D(2\pi/L)^2 n_x^2+|\omega_j|}-\frac{1}{D(2\pi/L)^2\left(n_x+2\phi/\phi_0\right)^2+|\omega_j|}\right) \\
&=\frac{1}{D(2\pi/L)^2}\sum_{n_x=-\infty}^{\infty}\left(\frac{-1}{(in_x)^2-\alpha_j^2}-\frac{-1}{(in_x+2i\varphi)^2-\alpha_j^2}\right),
\end{aligned} \tag{C.1}$$

where we defined $\alpha_j^2 \equiv |\omega_j|\,(L/2\pi)^2/D$ and $\varphi \equiv \phi/\phi_0$. To do this summation, we use Poisson summation formula which states that, for a given function $f(z)$,

$$\sum_{n=-\infty}^{\infty} f(in) = i\int_C dz \frac{f(z)}{e^{2\pi z}-1}, \tag{C.2}$$

where the contour for this integral is shown in Fig. 38.

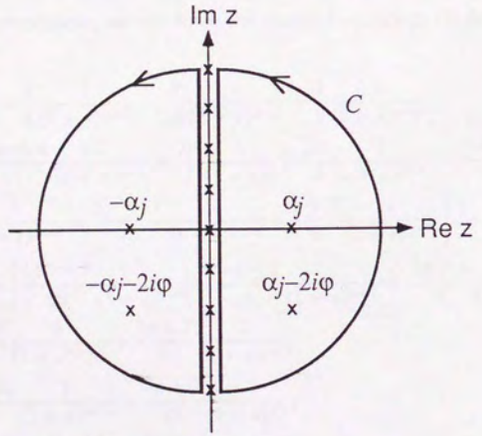

Fig. 38 Contour for the integral Eq. (C.2).

By use of Eq. (C.2), we evaluate the second term of the last line in the summation

Eq. (C.1).

$$\begin{aligned}
\sum_{n_x=-\infty}^{\infty}\frac{-1}{(in_x+2i\phi/\phi_0)^2-\alpha_j^2} &= i\int_C dz\frac{1}{e^{2\pi z}-1}\frac{-1}{(z+2i\varphi)^2-\alpha_j^2} \\
&=\frac{\pi}{\alpha_j}\frac{\sinh 2\pi\alpha_j}{\cosh 2\pi\alpha_j-\cos 4\pi\varphi}=\frac{\pi}{\alpha_j}\left(1+2\sum_{p=1}^{\infty}e^{-2\pi\alpha_j p}\cos 4\pi n\varphi\right),
\end{aligned} \tag{C.3}$$

where we used an expansion formula

$$\frac{1-x^2}{1-2x\cos\theta+x^2}=1+2\sum_{n=1}^{\infty}x^n\cos n\theta, \quad |\theta|\le\pi,\ |x|<1. \tag{C.4}$$

From Eq. (C.3), we obtain for the q summation (C.1) as

$$\sum_q\left(\tilde{D}-\tilde{C}\right)=\frac{1}{D(2\pi/L)^2}\frac{4\pi}{\alpha_j}\sum_{p=1}^{\infty}\sin^2 2\pi p\varphi e^{-2\pi\alpha_j p}. \tag{C.5}$$

Similarly we can obtain the q summations in Eqs. (5.13) and (5.23) as

$$\begin{aligned}
&\sum_q q^2\left(\tilde{D}^2\left(q,|\omega_j|\right)-\tilde{C}^2\left(q,|\omega_j|\right)\right) \\
&\qquad=\frac{1}{D^2(2\pi/L)^4}\frac{2\pi}{\alpha_j}\sum_{p=1}^{\infty}\left(1-2\pi p\alpha_j\right)\sin^2 2\pi p\varphi e^{-2\pi\alpha_j p},
\end{aligned} \tag{C.6}$$

and

$$\sum_q\tilde{C}^2\left(q,|\omega_j|\right)=\frac{1}{D^2(2\pi/L)^4}\frac{\pi}{2\alpha_j^3}\left[1+2\sum_{p=1}^{\infty}\left(1+2\pi p\alpha_j\right)\cos 4\pi p\varphi e^{-2\pi\alpha_j p}\right]. \tag{C.7}$$

References

1. C.P. Umbach, S. Washburn, R.B. Laibowitz, and R.A. Webb, Phys. Rev. B **30**, 4048 (1984).
2. Y. Gefen, Y. Imry, and M.Ya. Azbel, Phys. Rev. Lett. **52**, 129 (1984).
3. M. Büttiker, Y. Imry, R. Landauer, and S. Pinhas Phys. Rev. B **31**, 6207 (1985).
4. M. Büttiker, Y. Imry, and M.Ya. Azbel, Phys. Rev. A **30**, 1982 (1984).
5. R.A. Webb, S. Washburn, C.P. Umbach, and R.B. Laibowitz, Phys. Rev. Lett. **54**, 2696 (1985).
6. B.L. Altshuler, Pis'ma Zh. Eksp. Theor. Fiz. **41**, 530 (1985) [JETP Lett. **41**, 648 (1985)].
7. B.L. Altshuler and D.E. Khmelnitshii, Pis'ma Zh. Eksp. Theor. Fiz. **42**, 291 (1985) [JETP Lett. **42**, 359 (1986)].
8. B.L. Altshuler and Shklovskii, Zh. Eksp. Theor. Fiz. **91**, 220 (1986) [Sov. Phys. JETP **64**, 127 (1986)].
9. P. A. Lee and A. D. Stone, Phys. Rev. Lett. **55**, 1622 (1985).
10. P. A. Lee, A. D. Stone, and H. Fukuyama, Phys. Rev. B **35**, 1039 (1987).
11. C. L. Kane, R. A. Serota, and P. A. Lee, Phys. Rev. B **37**, 6701 (1988).
12. Y. Imry, Europhys. Lett. **1**, 249 (1986).
13. P.A. Mello, Phys. Rev. Lett. **60**, 1089 (1988).
14. S. Iida, H. A. Weidenmuller, and J. A. Zuk, Phys. Rev. Lett. **64**, 583 (1990); Ann. Phys.(USA), **200**, 219 (1990).
15. P.A. Mello and A.D. Stone, Phys. Rev. B **44**, 3559 (1991).
16. C. V. De Souza and T. R. Kirkpatrick, Phys. Rev. B **43**, 10132 (1991).
17. A.D. Stone, Phys. Rev. Lett. **54**, 2692 (1985).
18. N. Giordano, Phys. Rev. B **36**, 4190 (1987).
19. X.C. Xie and S. Das Sarma, Phys. Rev. B **38**, 3529 (1988).
20. K. Tankei, A. Sawada, and Y. Nagaoka, J. Phys. Soc. Jpn. **58**, 368 (1989).
21. B. Kramer, J. Masek, V. Spicka, and B. Velicky, Surf. Sci. **229**, 316 (1990).
22. R. Harris and A. Houari, Phys. Rev. B **41**, 5487 (1990).
23. S. Datta, M. Cahay, and M. McLennan, Phys. Rev. B **36**, 5655 (1987).
24. M. Cahay, M. McLennan, and S. Datta, Phys. Rev. B **37**, 10125 (1988).
25. M. Cahay, S. Bandyopadhyay, M.A. Osman, and H.L. Grubin, Surf. Sci. **228**, 301 (1990).
26. S. Bandyopadhyay, M. Cahay, D. Berman, and B. Nayfeh, in *Proceedings of the 5th International Conference on Superlattices and Microstructures, Berlin, 1990.*

27. H. Tamura and T. Ando, Phys. Rev. B **44**, 1792 (1991).
28. M. Büttiker, Y. Imry, and R. Landauer, Phys. Lett. **96A**, 365 (1983).
29. R. Landauer and M. Büttiker, Phys. Rev. Lett. **54**, 2049 (1985).
30. M. Büttiker, Phys. Rev. B **32**, 1846 (1985).
31. L. P. Levy, G. Dolan, J. Dunsmuir, and H. Bouchiat, Phys. Rev. Lett. **64**, 2074 (1990).
32. V. Chandrasekhar, R. A. Webb, M. J. Brady, M. B. Ketchen, W. J. Gallagher, and A. Kainsasser, Phys. Rev. Lett. **67**, 3578 (1991).
33. H. F. Cheung, Y. Gefen, E. K. Riedel, and W. H. Shih, Phys. Rev. B **37**, 6050 (1988).
34. H. Bouchiat and G. Montambaux, J. Phys. (Paris) **50**, 2695, 1989.
35. B. L. Altshuler, Y. Gefen, and Y. Imry, Phys. Rev. Lett. **66**, 88 (1991).
36. A. Schmid, Phys. Rev. Lett. **66**, 80 (1991).
37. F. von Oppen and E. K. Riedel, Phys. Rev. Lett. **66**, 84 (1991).
38. V. Ambegaokar and U. Eckern, Phys. Rev. Lett. **65**, 381 (1990).
39. H. F. Cheung, E. K. Riedel, and Y. Gefen, Phys. Rev. Lett. **62**, 587 (1989).
40. H. Yoshioka and H. Fukuyama, preprint.
41. E. K. Riedel and F. von Oppen, preprint.
42. U. Eckern and A. Schmid, Europhys. Lett. **18**, 457 (1992).
43. H. Tamura and H. Yoshioka, unpublished.
44. B.J. van Wees, H. van Houten, C.W.J. Beenekkar, J.G. Williamson, L.P. Kouwenhoven, D. van der Marel, and C.T. Foxon, Phys. Rev. Lett. **60**, 848 (1988).
45. D.A. Wharam, T.J. Thornton, R. Rewbury, M. Pepper, H. Ahmed, J.E.F. Frost, D.G. Hasko, D.C. Peacock, D.A. Ritchie, and G.A.C. Jones, J. Phys. C **21**, L209 (1988).
46. T. Ando and H. Tamura, Superlattices and Microstructures, **9**, 137 (1991).
47. T. Ando, H. Tamura, and H. Akera, *New Horizons in Low-Dimensional Electron Systems*, edited by H. Aoki *et al* (Kluwer Academic Publishers, Netherlands, 1992), p. 351.
48. T. Ando, H. Tamura, and H. Akera, *Science and Technology of Mesoscopic Structures*, edited by S. Namba *et al* (Springer-Verlag, Tokyo, 1992), p. 178.
49. T. Ando and H. Tamura, Phys. Rev. B **46**, 2332 (1992).
50. T. Ando, J. Phys. Soc. Jpn. **51**, 3900 (1982).
51. T. Ando and Y. Murayama, J. Phys. Soc. Jpn. **54**, 1519 (1985).
52. H. Sakaki, Jpn. J. Appl. Phys **19**, L735 (1980).
53. D.S. Fisher and P.A. Lee, Phys. Rev. B **23**, 6851 (1981).

54. M. Büttiker, Phys. Rev. Lett. **57**, 1761 (1986).
55. M. Büttiker, Phys. Rev. B **38**, 9375 (1988).
56. A.D. Stone and A. Szafer, IBM J. Res. Develop. **32**, 384 (1988).
57. H.U. Baranger and A.D. Stone, Phys. Rev. B **40**, 8169 (1989).
58. R. Landauer, IBM J. Res. Develop. **1**, 223 (1957); Phil. Mag. **21**, 863 (1970).
59. Y. Isawa, H. Ebisawa, and S. Maekawa, J. Phys. Soc. Jpn. **55**, 2523 (1986); S. Maekawa, Y. Isawa, and H. Ebisawa, J. Phys. Soc. Jpn. **56**, 25 (1987); Y. Isawa, H. Ebisawa, and S. Maekawa, in *Anderson Localization*, edited by T. Ando and H. Fukuyama (Springer-Verlag, Berlin, 1988), p. 329.
60. M. Büttiker, Phys. Rev. B **35**, 4123 (1987).
61. H.U. Baranger, A.D. Stone, and D.P. DiVincenzo, Phys. Rev. B **37**, 6521 (1988), C.L. Kane, P.A. Lee, and D.P. DiVincenzo, Phys. Rev. B **38**, 2995 (1988), D.P. DiVincenzo and C.L. Kane, Phys. Rev. B **38**, 3006 (1988),
62. S. Hershfield and V. Ambegaokar, Phys. Rev. B **38**, 7909 (1988). S. Hershfield, Ann. of Phys. **196**, 12 (1989).
63. A. Benoit, C.P. Umbach, R.B. Laibowitz, and R.A. Webb, Phys. Rev. Lett. **58**, 2343 (1987).
64. W.J. Skocpol, P.M. Mankiewich, R.E. Howard, L.D. Jackel, D.M. Tennant, and A.D. Stone, Phys. Rev. Lett. **58**, 2347 (1987).
65. P.W. Anderson, Phys. Rev. B **23**, 4828 (1981).
66. See, for example, Y.-C. Chang, and J.N. Schulman, Phys. Rev. B **25**, 3975 (1982); **31**, 2069 (1985), and references therein.
67. P.F. Bagwell, Phys. Rev. B **41**, 10354 (1990).
68. T. Ando and Y. Uemura, J. Phys. Soc. Jpn. **36**, 959 (1974).
69. T. Ando, J. Phys. Soc. Jpn. **36**, 1521 (1974); **37**, 622 (1974); **37**, 1233 (1974).
70. P.W. Anderson, D.J. Thouless, E. Abrahams, and D.S. Fisher, Phys. Rev. B **22**, 3519 (1980).
71. E. Abrahams and M.J. Stephen, J. Phys. C **13**, L377 (1980).
72. B.S. Andereck and E. Abrahams, J. Phys. C **13**, L383 (1980).
73. J. Sak and B. Kramer, Phys. Rev. B **24**, 1761 (1981).
74. A.D. Stone, J.D. Joannopoulos, and D.J. Chadi, Phys. Rev. B **24**, 5583 (1981).
75. A.A. Abrikosov, Physica Scripta **T27**, 148 (1989).
76. See, for example, H. Akera and T. Ando, Phys. Rev. B **41**, 11967 (1990).
77. T. Ando, Phys. Rev. B **42**, 5626 (1990).
78. T. Martin and S. Feng, Phys. Rev. Lett. **64**, 1971 (1990).
79. S. Komiyama, H. Hirai, S. Sasa, and T. Fujii, Solid State Commun. **73**, 91 (1990).

80. B.W. Alphenaar, P.L. McEuen, R.G. Wheeler, and R.N. Sacks, Phys. Rev. Lett. **64**, 677 (1990).
81. B.L. van Wees, E.M.M. Willems, L.P. Kouwenhoven, C.J.P.M. Harmans, J.G. Williamson, C.T. Foxon, and J.J. Harris, Phys. Rev. B **39**, 8066 (1989).
82. D.J. Thouless, J. Phys. C **6**, L49 (1973).
83. K.B. Efetov and A.I. Larkin, Zh. Eksp. Theor. Fiz. **85**, 764 (1983)[Sov. Phys. JETP **58**, 444 (1983)].
84. J.-L. Pichard, M. Sanquer, K. Slevin, and P. Debray, Phys. Rev. Lett. **65**, 1812 (1990).
85. A. MacKinnon and B. Kramer, Phys. Rev. Lett. **47**, 1546 (1981).
86. O.N. Dorokhov, Zh. Eksp. Theor. Fiz. **85**, 1040 (1983)[Sov. Phys. JETP **58**, 606 (1983)].
87. J. -L. Pichard, *Quantum Coherence in Mesoscopic Systems*, edited by B. Kramer (NATO ASI series, Plenum Press, New York, 1991), p. 369.
88. T. Ando, Phys. Rev. B **40**, 5326 (1989).
89. F. J. Ohkawa and Y. Uemura, J. Phys. Soc. Jpn. **37**, 1325 (1974).
90. T. J. Thornton, M. L. Roukes, A. Scherer, and B. P. van de Gaag, Phys. Rev. Lett. **63**, 2128 (1989).
91. K. Forsvoll and I. Holwech, Philos. Mag., **9**, 435 (1964).
92. A. B. Pippard, *Magnetoresistance in Metals* (Cambridge University Press, Cambridge, 1989), p.196-236.
93. H. Akera and T. Ando, Phys. Rev. B **43**, 11676 (1991).
94. H. Higurashi, S. Iwabuchi, and Y. Nagaoka, Surf. Sci. **263**, 382 (1992).
95. H. Fukuyama, J. Phys. Soc. Jpn. **49**, 649 (1980); J. Phys. Soc. Jpn. **50**, 3562 (1981).
96. D. G. Cantrell and P. N. Butcher, J. Phys. C **18**, 5111 (1985); J. Phys. C **18**, 6627 (1985).
97. M. J. Kearney and P. N. Butcher, J. Phys. C **20**, 47 (1987); J. Phys. C **21**, 2539 (1988).
98. S. Iwabuchi and Y. Nagaoka, J. Phys. Soc. Jpn. **58**, 1325 (1989); *Proceedings of 3rd International Symposium of Quantum Mechanics*, edited by S. Kobayashi, H. Ezawa Y. Murayama, and S. Nomura (Physical Society of Japan, Tokyo), p.288 (1989).
99. M. Suhrke, S. Wilke, andd R. Keiper, Solid State Commun. **76**, 551 (1909); M. Suhrke and S. Wilke, Phys. Rev. B **46**, 2400 (1992).
100. P.A. Mello and B. Shapiro, Phys. Rev. B **37**, 5860 (1988).
101. P.A. Mello, P. Pereyra, and N. Kumar, Annals of Phys. **181**, 290 (1988).

102. J.-L. Pichard, M. Sanquer, K. Slevin, and P.Debray, Phys. Rev. Lett. **65**, 1812 (1990).

103. J. -L. Pichard, P. A. Mello, A. D. Stone, and N. Zanon, Surf. Sci. **229**, 101 (1990).

104. H. Tamura and T. Ando, *Transport Phenomena in Mesoscopic Systems*, edited by H. Fukuyama and T. Ando (Springer-Verlag, Berlin, 1992), p. 117.

105. H. Tamura and T. Ando, Physica **B** (to appear).

106. P.A. Mello and J.-L. Pichard, J. Phys. France I **1**, 493 (1991).

107. M. Gaudin and P.A. Mello, J. Phys. G **7**, 1085 (1981); P.A. Mello, J. Phys. A **23**, 4061 (1990).

108. K.B. Efetov and A.I. Larkin, Zh. Eksp. Theor. Fiz. **85**, 764 (1983)[Sov. Phys. JETP **58**, 444 (1983)].